

Bifurcations of periodic orbits in the 3D secular planetary 3-Body problem: an approach through an integrable Hamiltonian system

Rita Mastroianni

Advanced Concept Team, European Space Agency, European Space Technology and Research Centre
Keplerlaan 1, 2201 AZ Noordwijk

Antonella Marchesiello

Department of Applied Mathematics, Faculty of Information Technology, Czech Technical University in Prague,
Thákurova 9, 160 00 Prague

Christos Efthymiopoulos

Dipartimento di Matematica “Tullio Levi-Civita”, Università degli Studi di Padova,
via Trieste 63, 35121 Padova,

Giuseppe Pucacco

Dipartimento di Fisica, Università degli Studi di Roma “Tor Vergata”,
via della Ricerca Scientifica 1, 00133 Roma,

e-mails: rita.mastroianni@esa.int, marchant@fit.cvut.cz
cefthym@math.unipd.it, pucacco@roma2.infn.it

Abstract

We analyze, through a geometric description, the sequence of bifurcations of periodic orbits in a Hamiltonian model derived from the normalization of the secular 3D planetary three body problem. Stemming from the results in [12], we analyze the phase space of the corresponding integrable approximation. In particular, we propose a normal form leading to an integrable Hamiltonian whose sequence of bifurcations is qualitatively the same as that in the complete system. Using as representation of the phase space the 3D-sphere in the Hopf variables space ([6], [3], [11]), we geometrically analyze phase-space dynamics through the sequence of bifurcations leading to the appearance of fixed points of the secular Hamiltonian flow, i.e., periodic orbits in the complete system. Moreover, through a semi-analytical method, we find the critical values of the second integral giving rise to pitchfork and saddle-node bifurcations characterising the dynamics.

1 Introduction

The model derives from a classical problem of Celestial Mechanics. We start from the planetary three body problem in Poincaré heliocentric canonical variables governed by the Hamiltonian

$$\mathcal{H}(\mathbf{r}_2, \mathbf{r}_3, \mathbf{p}_2, \mathbf{p}_3) = \frac{\mathbf{p}_2^2}{2m_2} - \frac{\mathcal{G}m_0m_2}{r_2} + \frac{\mathbf{p}_3^2}{2m_3} - \frac{\mathcal{G}m_0m_3}{r_3} + \frac{(\mathbf{p}_2 + \mathbf{p}_3)^2}{2m_0} - \frac{\mathcal{G}m_2m_3}{|\mathbf{r}_2 - \mathbf{r}_3|}, \quad (1)$$

where $m_0 \gg m_2, m_3$. Thus m_0 represents the mass of a ‘star’, and $m_i, \mathbf{p}_i, \mathbf{r}_i, i = 2, 3$ the masses, barycentric momenta and heliocentric position vectors of two ‘planets’ orbiting the star, at distances

$r_i = |\mathbf{r}_i|$. A systematic study of how the structure of the phase space of the above Hamiltonian system is altered as the planetary masses and distances and, most importantly, the mutual inclination between the two planets' trajectories is varied is shown in [12]. A well-studied case of the latter is the ν -Andromedæ system, that is a double star system with four planets (**b**, **c**, **d** and **e**) orbiting one of the stars. Since the masses m_c and m_d are much larger than m_b , m_e , the system is reconducted to a 3-body problem since the planets **c**, **d** are the ones providing the main perturbations of the system. Following the formalism introduced in that work, we arrive at a natural decomposition of the 3D secular Hamiltonian of a system with fixed Angular Momentum Deficit (AMD; see [7]) as

$$\mathcal{H}_{sec} = \mathcal{H}_{planar}(\mathbf{X}, \mathbf{Y}) + \mathcal{H}_{space}(\mathbf{X}, \mathbf{Y}; \text{AMD}) \quad . \quad (2)$$

In Eq. (2), (\mathbf{X}, \mathbf{Y}) are Poincaré canonical variables for the two planets ((X_2, Y_2) , (X_3, Y_3) are essentially proportional to the planets' eccentricity vectors). The Angular Momentum Deficit is an integral of motion defined as

$$\text{AMD} = L_2 + L_3 - L_z \quad (3)$$

where L_2 , L_3 are the angular momenta of the circular orbits at semi-major axes a_2 , a_3 equal to those of the two planets, and L_z the modulus of the total angular momentum normal to the system's Laplace plane. The Hamiltonian \mathcal{H}_{space} can be further decomposed as $\mathcal{H}_{space} = \mathcal{H}_{0,space} + \mathcal{H}_{1,space}$, where $\mathcal{H}_{0,space}$ also admits $\sigma_0/2 = (X_2^2 + Y_2^2 + X_3^2 + Y_3^2)/4$ as a second integral. Then, the Hamiltonian

$$\mathcal{H}_{int} = \mathcal{H}_{planar} + \mathcal{H}_{0,space} \quad (4)$$

is integrable with a formal structure similar to that of \mathcal{H}_{planar} . Concerning \mathcal{H}_{planar} , it admits two periodic orbits (called below the 'modes' A and B) which correspond to the anti-aligned and aligned apsidal corotation states (see, for example, [8], [1], [9]) for the two planets in the planar case. Physically, they represent periodic orbits along which the pericenters of the two planets constantly precess by remaining either always anti-aligned (state A) or always aligned (state B). Furthermore, the existence of periodic orbits of the type A and B can be demonstrated also for the Hamiltonian \mathcal{H}_{int} using its integrability property, in the same way as for \mathcal{H}_{planar} . In this case, the A and B mode are the continuation of those of the planar case, representing families of off-plane periodic orbits.

Our aim is to understand the dynamics of \mathcal{H}_{sec} , the non-integrable 'complete' model. Therefore, we focus on integrable Hamiltonian approximation models, analysing the possible bifurcations of the integrable counterpart. Indeed, we will see that, apart from the apsidal corotations, other bifurcations are a-priori possible, as saddle-node or pitchfork bifurcations. However, considering only the integrable part of the Hamiltonian, it is not always sufficient to reproduce the same dynamics as the complete system. Inspired by the case studied in [12], in which orbital parameters compatible with those observed in the ν -Andromedæ system are considered, we show in numerical example that the integrable approximation of the Hamiltonian \mathcal{H}_{int} (Eq. (4)) does not exhibit the same sequence of bifurcations as the one produced by the complete secular Hamiltonian (Eq. (2)). For this reason, we introduce a *normal form* leading to an integrable Hamiltonian whose sequence of bifurcations is qualitatively the same as the one of the complete system. Exploiting the normal-form Hamiltonian, we perform a geometrical description of inequivalent classes of sequence of bifurcations and determine semi-analytical formulæ to find critical values of the formal second integral σ_0 giving rise to both pitchfork and saddle-node bifurcations.

The work is organized as follow. In Section 2 we briefly recall how to determine the secular Hamiltonian for the spatial three body problem (3BP) and how to decompose the different contributions.

At the beginning of Section 3 we report the study of the Poincaré surface of section for the complete secular 3BP Hamiltonian for different levels of energy \mathcal{E} . Section 3.2 is devoted to the integrable part of the Hamiltonian, \mathcal{H}_{int} : in Section 3.2.1 we determine the phase space structure of the integrable Hamiltonian as obtained by i) the Poincaré surface of section, for different levels of energy \mathcal{E} , and, analogously, ii) by the contour plots, considering different values of the integral σ_0 . The sequence of bifurcations is geometrically analyzed in Section 3.2.2. Instead, Section 3.3 is dedicated to the normalized integrable Hamiltonian: more precisely, it contains the formal construction of the normal form and the geometrical analysis of the sequence of bifurcations produced by the correspondent normalized integrable Hamiltonian. Finally, in Section 4, we consider a lower-order of approximation of the present Hamiltonian (with respect both the multipolar order of truncation and expansion in power of eccentricity and inclination). More precisely, given a generic integrable Hamiltonian of the form (36), in Section 4.1 we report the formulæ leading to the *bifurcation values* of the integral σ_0 for which a critical point of the *first or second kind* occur. Sections 4.2.1 and 4.2.2 are devoted, respectively, to the study of the integrable and normalized integrable octupolar approximation of the Hamiltonian. In this section a geometrical analysis of the produced sequence of bifurcations is included. Finally, Section 5 is devoted to the conclusions.

2 Hamiltonian model

Following section 2.2 of [12], we derive the secular model \mathcal{H}_{sec} for the Hamiltonian (1) by performing averaging with respect to the fast angles just ‘by scissors’. We denote by $(a, e, i, M, \omega, \Omega)$ the Keplerian elements of a body (semi-major axis, eccentricity, inclination, mean anomaly, argument of the periastron, argument of the nodes), and by $\lambda = M + \omega + \Omega$, $\varpi = \omega + \Omega$ the mean longitude and longitude of the periastron respectively. The secular model is obtained averaging \mathcal{H} with respect to the fast angles M_2, M_3 :

$$\begin{aligned} \mathcal{H}_{sec} &= \frac{1}{4\pi^2} \int_0^{2\pi} \int_0^{2\pi} \mathcal{H}(\mathbf{r}_2, \mathbf{r}_3, \mathbf{p}_2, \mathbf{p}_3) dM_2 dM_3 \\ &= -\frac{\mathcal{G}m_0m_2}{2a_2} - \frac{\mathcal{G}m_0m_3}{2a_3} + \frac{\mathcal{G}m_2^2}{2a_2} + \frac{\mathcal{G}m_3^2}{2a_3} - \frac{\mathcal{G}m_2m_3}{a_3} + \mathcal{R}_{sec}(a_2, a_3, e_2, e_3, i_2, i_3, \omega_2, \omega_3, \Omega_2 - \Omega_3), \end{aligned} \quad (5)$$

where

$$\mathcal{R}_{sec} = \frac{1}{4\pi^2} \int_0^{2\pi} \int_0^{2\pi} -\frac{\mathcal{G}m_2m_3}{r_3} \left(-\frac{1}{2} \frac{r_2^2}{r_3^2} + \frac{3}{2} \frac{(\mathbf{r}_2 \cdot \mathbf{r}_3)^2}{r_3^4} + \dots \right) dM_2 dM_3. \quad (6)$$

We recall that keeping only the lowest order term in the integrand of (6), proportional to $(r_2/r_3)^2$, leads to the so-called *quadrupole* approximation; the next truncation (up to terms proportional to $(r_2/r_3)^3$) is the *octupole* approximation, etc. The integrals of any multipole approximation can be computed in so-called *closed form* (i.e. without expansions in the eccentricities), by avoiding completely the series reversion of Kepler’s equation, using, instead, the change of variables $M_2 \rightarrow u_2$ (eccentric anomaly), $M_3 \rightarrow f_3$ (true anomaly).

We continue following the description of Section 2.3 of [12]. Thus, after the introduction of the ‘book-keeping symbol’ (keeping track of the order in eccentricity and in the mutual inclination) and after having performed the Jacobi’s reduction of the nodes, we arrive at the following natural decomposition of the Hamiltonian:

$$\mathcal{H}_{sec}(w_2, w_3, W_2, W_3; L_z) = \mathcal{H}_{planar}(w_2 - w_3, W_2, W_3) + \mathcal{H}_{space}(w_2, w_3, W_2, W_3; L_z), \quad (7)$$

where

$$\begin{aligned}
L_j &= m_j \sqrt{\mathcal{G} m_0 a_j}, & l_j &= M_j, \\
G_j &= L_j \sqrt{1 - e_j^2}, & g_j &= \omega_j, \\
H_j &= G_j \cos(i_j), & h_j &= \Omega_j,
\end{aligned} \tag{8}$$

are the Delaunay canonical variables and

$$\begin{aligned}
\Lambda_j &= L_j, & \lambda_j &= M_j + \omega_j + \Omega_j, \\
W_j &= L_j - G_j, & w_j &= -\omega_j,
\end{aligned} \tag{9}$$

correspond to the modified-Delaunay variables, with $j = 2, 3$.

Moreover, the spatial part, namely \mathcal{H}_{space} , can be splitted into those terms which depend only on the difference $w_2 - w_3 = \omega_3 - \omega_2$, denoted by $\mathcal{H}_{0,space}$, and those which depend also on the other possible combinations, denoted by $\mathcal{H}_{1,space}$. Thus, we finally arrive at the following decomposition of the Hamiltonian

$$\mathcal{H}_{sec} = \underbrace{\mathcal{H}_{planar}(w_2 - w_3, W_2, W_3) + \mathcal{H}_{0,space}(w_2 - w_3, W_2, W_3; L_z)}_{\text{Integrable part} := \mathcal{H}_{int}} + \mathcal{H}_{1,space}(w_2, w_3, W_2, W_3; L_z). \tag{10}$$

The first two terms in the above expression give rise to a 2 degrees of freedom integrable Hamiltonian

$$\mathcal{H}_{int}(w_2 - w_3, W_2, W_3; \text{AMD}) = \mathcal{H}_{planar}(w_2 - w_3, W_2, W_3) + \mathcal{H}_{0,space}(w_2 - w_3, W_2, W_3; \text{AMD}), \tag{11}$$

(where the AMD is defined as in Eq. (3)), whose second integral is $W_2 + W_3$.

3 Poincaré surface of section

In the following sections we will show the Poincaré surface of section for different Hamiltonian models, i.e., considering different multipolar order of expansion and considering different integrable approximation of the Hamiltonian function. In all the numerical examples which follow, we refer to the mass, periods and AMD parameters as estimated for the v -Andromedæ system, explicitly reported at the beginning of Section 2.4 of [12].

3.1 The case of the secular Hamiltonian

We start by defining the Poincaré surface of section $\mathcal{P}(\mathcal{E}; \text{AMD})$ of \mathcal{H}_{sec} by means of the relations:

$$\mathcal{P}_{sec}(\mathcal{E}; \text{AMD}) = \left\{ (X_2, Y_2, X_3, Y_3) \in \mathbb{R}^4 : \mathcal{H}_{sec}(X_2, Y_2, X_3, Y_3 = 0; \text{AMD}) = \mathcal{E}, Y_3 = 0, \right. \\
\left. \dot{Y}_3 = -\frac{\partial \mathcal{H}_{sec}}{\partial X_3} \Big|_{Y_3=0} \geq 0, \cos(i_{max}) \leq \cos(i_{mut})(X_2, Y_2, X_3, Y_3 = 0; \text{AMD}) \leq 1 \right\}, \tag{12}$$

where the mutual inclination $i_{mut} = i_2 + i_3$ for fixed AMD, or angular momentum $L_z = \Lambda_2 + \Lambda_3 - \text{AMD}$, is given by

$$\cos(i_{mut}) = \frac{L_z^2 - \Lambda_2^2 - \Lambda_3^2 + \Lambda_2^2 e_2^2 + \Lambda_3^2 e_3^2}{2\Lambda_2 \Lambda_3 \sqrt{1 - e_2^2} \sqrt{1 - e_3^2}} = \frac{L_z^2 - G_2^2 - G_3^2}{2G_2 G_3} \tag{13}$$

and the maximum possible mutual inclination consistent with the given AMD is

$$i_{max} = \cos^{-1} \left(\frac{L_z^2 - \Lambda_2^2 - \Lambda_3^2}{2\Lambda_2\Lambda_3} \right) . \quad (14)$$

Moreover, (X_j, Y_j) are the Poincaré canonical variables (coordinates momenta), stemming from the variables (w_j, W_j) , through the canonical transformation

$$X_j = -\sqrt{2W_j} \cos(w_j), \quad Y_j = \sqrt{2W_j} \sin(w_j), \quad j = 2, 3 . \quad (15)$$

The phase portrait corresponding to the Poincaré surface of section *at a fixed level of energy* \mathcal{E} is obtained numerically, by choosing several initial conditions $(X_2, Y_2) \in \mathcal{D}(\mathcal{E}) \subset \mathbb{R}^2$, where $\mathcal{D}(\mathcal{E})$ is the domain of permissible initial conditions consistent with the definition of the surface of section as defined in Eq. (12). For each initial conditions, we then iterate the corresponding orbit under the Hamiltonian \mathcal{H}_{sec} , and plot the consequent points (X_2, Y_2) .

Figure 1 shows a summary of our basic example of computation of phase portraits, in the form of Poincaré surfaces of section computed as explained above. Section 2.4.2 of [12] shows different precision tests, i.e., for models differing in the maximum multipole degree N_P up to which the original Hamiltonian \mathcal{H} is expanded, before the averaging, as well as in the maximum order in book-keeping N_{bk} of the Hamiltonian \mathcal{H}_{sec} , which is also equal to the maximum order at which the eccentricities appear in \mathcal{H}_{sec} . In this case, we fix $N_P = 5$ and $N_{bk} = 12$. In particular, Fig. 1 shows the same sequence of bifurcations already observed in Figs. 5 and 9 of [12] for different multipolar N_P and book-keeping N_{bk} orders.¹

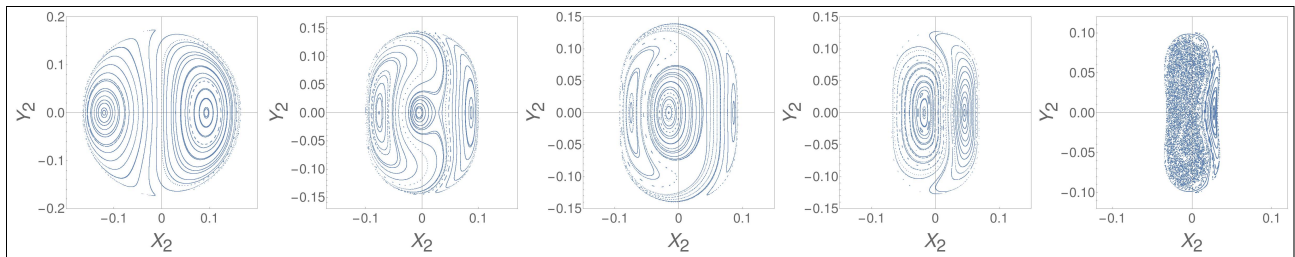


Figure 1: Poincaré surfaces of section $\mathcal{P}_{sec}(\mathcal{E}; \text{AMD})$ in the plane (X_2, Y_2) with L_z fixed and different values of energy. The surfaces of section are computed by a numerical integration of trajectories in the Hamiltonian truncated at multipolar degree $N_P = 5$, order $N_{bk} = 12$ in the eccentricities, and energies (from left to right) $\mathcal{E} = -6.77 \cdot 10^{-5}, -2.53 \cdot 10^{-5}, -2.16 \cdot 10^{-5}, -1.17 \cdot 10^{-5}, -2.61 \cdot 10^{-6}$.

3.2 The case of the integrable Hamiltonian

In this work we want to focus on the integrable part of the Hamiltonian, namely \mathcal{H}_{int} , in order to analyze and semi-analytically determine its periodic orbits. Thus, we start computing the Poincaré

¹Note that, in this case, the Poincaré surfaces of section are represented in the plane (X_2, Y_2) and not in $(e_2 \cos(\omega_2), e_2 \sin(\omega_2))$. Recalling that $e_2 = \left(1 - \left(1 - \frac{(X_2^2 + Y_2^2)}{2\Lambda_2}\right)^2\right)^{1/2}$ and $\omega_2 = \text{sgn}\left(\frac{-Y_2}{\sqrt{X_2^2 + Y_2^2}}\right) \arccos\left(\frac{-X_2}{\sqrt{X_2^2 + Y_2^2}}\right)$, it is easy to recognise the same sequence of bifurcations.

surface of section $\mathcal{P}_{int}(\mathcal{E}; \text{AMD})$, i.e., at a fixed level of energy and considering only \mathcal{H}_{int} instead of the full \mathcal{H}_{sec} .² They are reported in Figure 2.

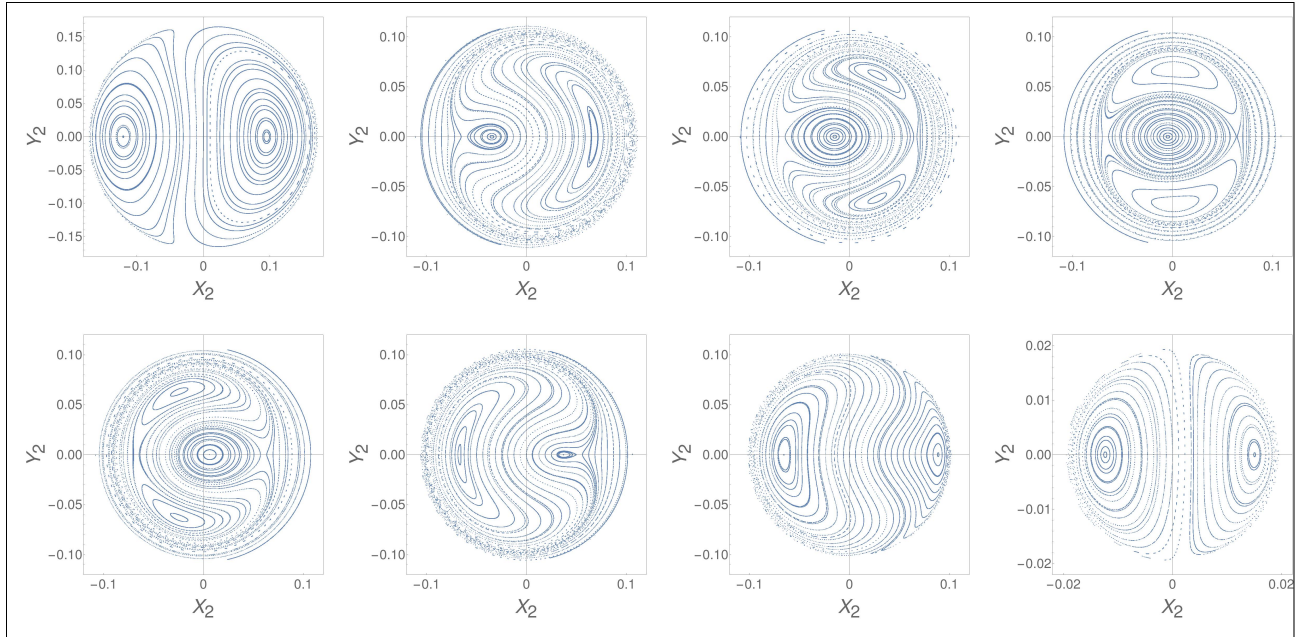


Figure 2: Poincaré surfaces of section $\mathcal{P}_{int}(\mathcal{E}; \text{AMD})$ in the plane (X_2, Y_2) with L_z fixed and different values of energy. The surfaces of section are computed by a numerical integration of trajectories of the integrable part of the Hamiltonian truncated at multipolar degree $N_P = 5$, order $N_{bk} = 12$ in the eccentricities. The values of the energies (from top to bottom, from left to right) are taken as $\mathcal{E} = -6.77 \cdot 10^{-5}, -1.8 \cdot 10^{-5}, -1.74 \cdot 10^{-5}, -1.7 \cdot 10^{-5}, -1.67 \cdot 10^{-5}, -1.6 \cdot 10^{-5}, -1.43 \cdot 10^{-5}, -4.05 \cdot 10^{-7}$. In this case the values of the energy for which we can have co-planar orbits are $\mathcal{E}_{min} = -1.18 \cdot 10^{-4}$ and $\mathcal{E}_{2,3} = -6.77 \cdot 10^{-5}$. We start consider values of the energy $\mathcal{E} \geq \mathcal{E}_{2,3}$ for which the Poincaré sections are complete, without prohibited domains (see [12]).

3.2.1 Phase portraits for the integrable Hamiltonian

We define the following canonical transformation

$$\begin{aligned} \psi &= w_2 - w_3, & \Gamma &= \frac{W_2 - W_3}{2}, \\ \varphi &= w_2 + w_3, & J &= \frac{W_2 + W_3}{2}. \end{aligned} \quad (16)$$

The Hamiltonian in the new variables reads (apart from a constant)

$$\mathcal{H}_{sec}(\psi, \varphi, \Gamma, J) = \mathcal{H}_{int}(\psi, \Gamma; J) + \mathcal{H}_{1,space}(\psi, \varphi, \Gamma, J). \quad (17)$$

Thus, as we can see, \mathcal{H}_{int} is a one degree of freedom Hamiltonian in the variables (ψ, Γ) , with J serving as parameter. For this reason, instead of considering the Poincaré surface of section, obtained

²The variables N_P and N_{bk} are fixed, respectively, equal to 5 and 12, as before. This means that, the integrable Hamiltonian is a polynomial function of degree 12 in the Poincaré variables (\mathbf{X}, \mathbf{Y}) , or, equivalently, of degree 6 in the Hopf variables, cf. (18).

by numerical integrations, *at fixed level of energy* \mathcal{E} , it is possible to determine the continuous flow of \mathcal{H}_{int} in the variables (ψ, Γ) *at fixed value of the parameter* J .

Equivalently, we can introduce the Hopf variables $(\sigma_1, \sigma_2, \sigma_3)$ defined by:

$$\sigma_1 = X_2 X_3 + Y_2 Y_3, \quad \sigma_2 = Y_2 X_3 - Y_3 X_2, \quad \sigma_3 = \frac{1}{2} (X_2^2 + Y_2^2 - X_3^2 - Y_3^2), \quad (18)$$

satisfying the Poisson algebra $\{\sigma_i, \sigma_j\} = -2 \epsilon_{ijk} \sigma_k$, where ϵ_{ijk} is the Levi-Civita symbol and $i, j, k = 1, 2, 3$. Furthermore, we introduce the variable

$$\sigma_0 = \frac{1}{2} (X_2^2 + Y_2^2 + X_3^2 + Y_3^2) \quad (19)$$

which is a Casimir invariant of the previous algebra, since all Poisson brackets $\{\sigma_i, \sigma_0\}$, $i = 1, 2, 3$, vanish. From the definition (18) it follows that

$$\begin{aligned} \sigma_1 &= 2\sqrt{J+\Gamma}\sqrt{J-\Gamma}\cos(\psi), & \sigma_2 &= -2\sqrt{J+\Gamma}\sqrt{J-\Gamma}\sin(\psi), \\ \sigma_3 &= W_2 - W_3 = 2\Gamma. \end{aligned} \quad (20)$$

We also have the relation $\sigma_0 = W_2 + W_3 = 2J$, as well as

$$\sigma_1^2 + \sigma_2^2 + \sigma_3^2 = \sigma_0^2 = 4J^2. \quad (21)$$

Then, given the values of $(\sigma_1, \sigma_2, \sigma_3)$, the values of Γ , J and ψ can be computed unequivocally using the relations (20) and (21). Furthermore, it is easy to prove that $\mathcal{H}_{int} = \mathcal{H}_{int}(\sigma_1, \sigma_3; \sigma_0)$, i.e. the Hamiltonian \mathcal{H}_{int} does not depend on σ_2 . This implies that, fixing a value of σ_0 (i.e. of the integral J), the continuous in time phase flow obtained by solving the equations

$$\dot{\sigma}_1 = \{\sigma_1, \sigma_3\} \frac{\partial \mathcal{H}_{int}}{\partial \sigma_3}, \quad \dot{\sigma}_2 = \{\sigma_2, \sigma_1\} \frac{\partial \mathcal{H}_{int}}{\partial \sigma_1} + \{\sigma_2, \sigma_3\} \frac{\partial \mathcal{H}_{int}}{\partial \sigma_3}, \quad \dot{\sigma}_3 = -\{\sigma_1, \sigma_3\} \frac{\partial \mathcal{H}_{int}}{\partial \sigma_1}, \quad (22)$$

yields a flow equivalent to the one obtained under the Hamiltonian $\mathcal{H}_{int}(\psi, \Gamma; J)$, i.e., treating J as a parameter. Due to the constrain on the sphere (Eq. (21)), the curves of the flow (22) are given by the intersection of the constant energy surface $\mathcal{H}_{int}(\sigma_1, \sigma_3; \sigma_0) = \mathcal{E}$ with the sphere, i.e., they are closed curves which can be mapped to invariant curves in the plane (ψ, Γ) . These are geometrically equivalent to the invariant curves of the Poincaré surface of section of \mathcal{H}_{int} treated as a 2DOF system, mapping (X_2, Y_2) as $X_2 = -\sqrt{2(\Gamma + J)} \cos(\psi - \pi)$, $Y_2 = \sqrt{2(\Gamma + J)} \sin(\psi - \pi)$. It should be stressed, however, that the above Hamiltonian reduction only yields a geometric equivalence of the two curves, since in the 1DOF reduced system the flow is continuous, while in the 2DOF full system the curves are traced stroboscopically, and they correspond to the intersection of the 2D invariant tori involving both the angles (ψ, φ) with the selected surface of section. Thus, the question now is if, considering J , or σ_0 , as parameters, the corresponding phase portraits of the Poincaré surface of sections obtained for fixed values of the energy \mathcal{E} and shown in Fig. 2, lead to the same sequence of bifurcations. Looking at Fig. 4 we can establish the equivalence between the two methods. More precisely, Section 2.4 of [12] explains how to compute the range $\mathcal{E} \in [\mathcal{E}_{min}, \mathcal{E}_{max} = 0]$ and the corresponding non-null domain of definition $\mathcal{D}(\mathcal{E})$ for the Poincaré surface of sections. Moreover, looking at Fig. 11 of the same work, we can realize that, for each fixed value of the energy \mathcal{E} (i.e., for each Poincaré surface of section), there exist a minimal and a maximal value for σ_0 , i.e. the radius of the sphere. In this way, it is possible to determine a correspondence between \mathcal{E} and σ_0 . Thus, as shown in Fig. 3 of the present work, it is

possible to i) determine the range of definition of σ_0 , i.e., $\sigma_0 \in [\sigma_{0min}, \sigma_{0max}]$ and ii) for each (fixed) value of σ_0 , determine the minimal and maximal values for the energy, namely $[\mathcal{E}_{min\sigma_0}, \mathcal{E}_{max\sigma_0}]$. In particular, we stress the fact that each curve in the phase portrait at a fixed value of σ_0 (i.e. the panels shown in Fig. 4), correspond to a different level of energy. Finally, we observe that for each value of the energy $\mathcal{E} \in [\mathcal{E}_{min}, \mathcal{E}_{2,3}]$ there exist an unique allowed value of the radius σ_0 . More precisely, correspondently to $\sigma_0 = \sigma_{0max}$, the ‘curve’ at energy $\mathcal{E} = \mathcal{E}_{min}$ and $\mathcal{E} = \mathcal{E}_{2,3}$ will represent co-planar orbits, since \mathcal{E}_{min} and $\mathcal{E}_{2,3}$ have been computed so to have mutual inclination $i_{mut} = 0^\circ$ (see [12]). More precisely, they correspond, respectively, to the modes A and B (that will be introduced in the following), namely the anti-aligned and aligned apsidal corotations.

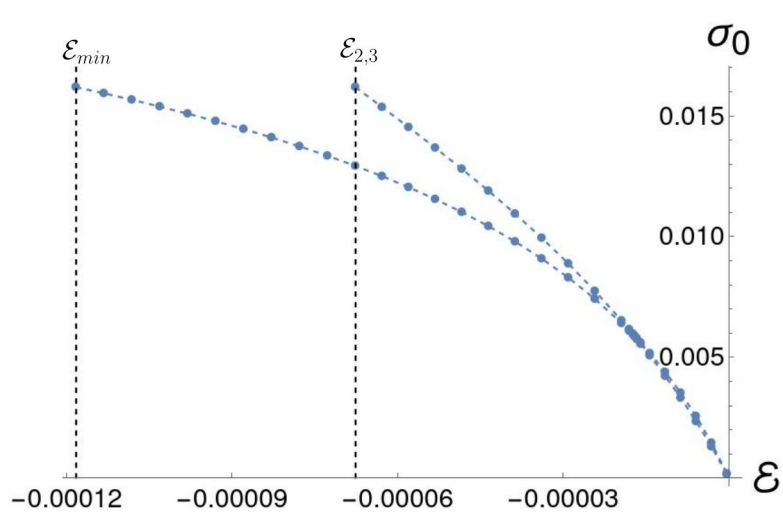


Figure 3: Correspondence between the energy \mathcal{E} and σ_0 . This allows to determine $\sigma \in [\sigma_{0min}, \sigma_{0max}]$. In this case (i.e. considering the Hamiltonian \mathcal{H}_{int} and $N_P = 5$, $N_{bk} = 6$, as in Fig. 2) correspondently to both $\mathcal{E}_{min} = -1.18 \cdot 10^{-4}$ and $\mathcal{E}_{2,3} = -6.77 \cdot 10^{-5}$, we compute $\sigma_{0max} = 0.0162044$.

Thus, it is possible now to determine the phase portraits for $\mathcal{H}_{int}(\sigma_1, \sigma_3; \sigma_0)$ at a fixed level of σ_0 , for $\sigma_0 \in [\sigma_{0min}, \sigma_{0max}]$. In order to compare the pictures with those reported in Fig. 2, we represent the phase portraits in the plane (X_2, Y_2) . To this end, it is sufficient to replace in $\mathcal{H}_{int}(\sigma_1, \sigma_3; \sigma_0)$ the values of σ_1 and σ_3 with their definition (18), and recall that $Y_3 = 0$ and $X_3 = \sqrt{2\sigma_0 - X_2^2 - Y_2^2}$ (by (19), (15) and the condition of section $\omega_3 = \pi$) so to have $\mathcal{H}_{int}(X_2, Y_2; \sigma_0)$. Thus, for each fixed value of $\sigma_0 \in [\sigma_{0min}, \sigma_{0max}]$, it is possible to compute the curves $\mathcal{H}_{int}(X_2, Y_2; \sigma_0) = \mathcal{E}$, with $\mathcal{E} \in [\mathcal{E}_{min\sigma_0}, \mathcal{E}_{max\sigma_0}]$, meaning that each curves of a single panel of Fig. 4 correspond to a different level of energy.

3.2.2 Geometrical analysis of the fixed points of the integrable Hamiltonian

As discussed in [12], using the Hopf variables it is possible to compute the periodic orbits of \mathcal{H}_{int} by geometrical considerations. More precisely, let

$$\mathcal{S}_{\sigma_0} = \{(\sigma_1, \sigma_2, \sigma_3) \in \mathbb{R}^3 : \sigma_1^2 + \sigma_2^2 + \sigma_3^2 = \sigma_0^2\} \quad (23)$$

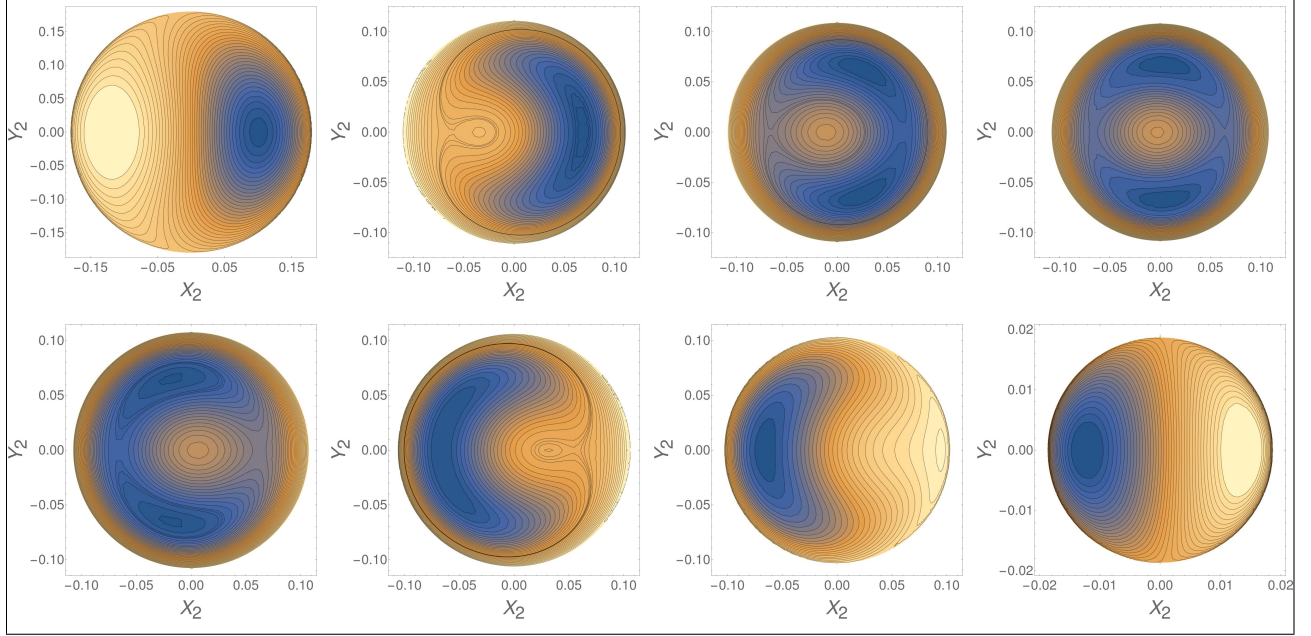


Figure 4: Contour plots, correspondent to $Y_3 = 0, \dot{Y}_3 \geq 0$, of $\mathcal{H}_{int}(X_2, Y_2; \sigma_0) = \mathcal{E}$ in the plane (X_2, Y_2) , with Hamiltonian \mathcal{H} truncated at multipolar degree $N_P = 5$, at order $N_{bk} = 12$ in the eccentricities, and decreasing values of σ_0 (from top to bottom, from left to right) $\sigma_0 = 1.62 \cdot 10^{-2}, 6.15 \cdot 10^{-3}, 5.93 \cdot 10^{-3}, 5.85 \cdot 10^{-3}, 5.78 \cdot 10^{-3}, 5.62 \cdot 10^{-3}, 5.304 \cdot 10^{-3}, 1.74 \cdot 10^{-4}$.

be the sphere corresponding to the fixed value σ_0 and

$$\mathcal{C}_{\sigma_0, \mathcal{E}} = \{(\sigma_1, \sigma_2, \sigma_3) \in \mathbb{R}^3 : \mathcal{H}_{int}(\sigma_0, \sigma_1, \sigma_3) = \mathcal{E}\}, \quad (24)$$

denoting the energy surface in the space $(\sigma_1, \sigma_2, \sigma_3) \in \mathbb{R}^3$, corresponding to an energy value \mathcal{E} . In this work we fix the value of σ_0 and we look for intersections between \mathcal{S}_{σ_0} and $\mathcal{C}_{\sigma_0, \mathcal{E}}$ for different values of the energy \mathcal{E} . Since \mathcal{H}_{int} does not depend on σ_2 , the constant energy surface $\mathcal{C}_{\sigma_0, \mathcal{E}}$ is normal to any plane (σ_1, σ_3) with $\sigma_2 = \text{const}$. At a non-degenerate tangency point of \mathcal{S}_{σ_0} with $\mathcal{C}_{\sigma_0, \mathcal{E}}$ we necessarily have the tangency condition

$$\text{rank} \begin{pmatrix} 2\sigma_1 & 2\sigma_2 & 2\sigma_3 \\ \frac{\partial \mathcal{H}_{int}}{\partial \sigma_1} & 0 & \frac{\partial \mathcal{H}_{int}}{\partial \sigma_3} \end{pmatrix} = 1, \quad ,$$

or equivalently, the rows of the above matrix do not vanish simultaneously and for some $\mu \in \mathbb{R}$

$$\nabla \mathcal{H}_{int} = \mu (\sigma_1, \sigma_2, \sigma_3). \quad (25)$$

This implies:

$$(\mu \neq 0) \quad \sigma_2 = 0, \quad \sigma_3 \frac{\partial \mathcal{H}_{int}}{\partial \sigma_1} = \sigma_1 \frac{\partial \mathcal{H}_{int}}{\partial \sigma_3}, \quad (26)$$

or

$$(\mu = 0) \quad \frac{\partial \mathcal{H}_{int}}{\partial \sigma_1} = \frac{\partial \mathcal{H}_{int}}{\partial \sigma_3} = 0. \quad (27)$$

In the first case (i.e. Eq. (26)) we have critical points (CP) of the first kind (CP1), while Eq. (27) identifies CP of the second kind (CP2), see [6]. Both cases imply that

$$\frac{\dot{\sigma}_1}{2} = \sigma_2 \frac{\partial \mathcal{H}_{int}}{\partial \sigma_3} = 0, \quad \frac{\dot{\sigma}_2}{2} = \sigma_3 \frac{\partial \mathcal{H}_{int}}{\partial \sigma_1} - \sigma_1 \frac{\partial \mathcal{H}_{int}}{\partial \sigma_3} = 0, \quad \frac{\dot{\sigma}_3}{2} = -\sigma_2 \frac{\partial \mathcal{H}_{int}}{\partial \sigma_1} = 0,$$

that is, the point of tangency is a fixed point of the flow.

Up to terms of second order in the variables σ_i (i.e. of fourth order in the eccentricities), we find

$$\mathcal{H}_{int} = A\sigma_1^2 + C\sigma_3^2 + B\sigma_1\sigma_3 + D(\sigma_0)\sigma_1 + E(\sigma_0)\sigma_3 + F(\sigma_0)$$

where A, B, C are constants, while the functions $D(\sigma_0)$ and $E(\sigma_0)$ are linear in σ_0 and $F(\sigma_0)$ contains terms linear and quadratic in σ_0 . In our numerical example the coefficients are given by:

$$\begin{aligned} A &= 0.00212824, & C &= 0.00186469, \\ B &= -0.00186482, & D(\sigma_0) &= 0.000165361 - 0.0159745 \sigma_0, \\ E(\sigma_0) &= 0.0000214817 - 0.00532338 \sigma_0, & F(\sigma_0) &= -0.00214065 \sigma_0 - 0.108446 \sigma_0^2. \end{aligned}$$

The quadratic form $A\sigma_1^2 + C\sigma_3^2 + B\sigma_1\sigma_3$ yields ellipses, being A, B, C such that $B^2 < 4AC$. Thus, for any permissible value \mathcal{E} , the surface $\mathcal{C}_{\sigma_0, \mathcal{E}}$ intersects the plane $\sigma_2 = 0$ along local ellipses-like curves (see the second and last row of Fig. 5).

Through the analysis of Fig. 5 we can discuss the sequence of bifurcations arising in the integrable approximation. In the first top frame of Fig. 5 we can see the presence of two fixed point of the flow, called A and B, and representing the basic *apsidal corotation orbits*. In particular, we find that \mathcal{S}_{σ_0} and $\mathcal{C}_{\sigma_0, \mathcal{E}}$ (where $\sigma_0 = \sigma_{0,max} = 1.62 \cdot 10^{-2}$) have two tangency points, called A and B, respectively for $\mathcal{E} = \mathcal{E}_{min}$ and $\mathcal{E} = \mathcal{E}_{2,3}$ (see caption of Figure 3). Moreover, it can be verified that $\psi^{(A)} = 0$ and $\psi^{(B)} = \pi$, leading to $\varpi_3 = \varpi_2 + \pi$ (perihelia anti-aligned) and $\varpi_3 = \varpi_2$ (perihelia aligned)³. Thus, the associated orbits yield two coplanar ellipses with, respectively, anti-aligned and aligned pericenters precessing with the same frequency. Decreasing the value of σ_0 (second frame on the top of Fig. 5), we can observe that a *saddle-node* bifurcation takes place, giving rise to two new fixed points of the Poincaré map, corresponding to periodic orbits called P_1 and P_2 . We can observe that the point P_1 is unstable, while P_2 is stable. They are given (same frame, bottom panel) by the tangency between the sphere \mathcal{S}_{σ_0} and the energy surfaces $\mathcal{C}_{\sigma_0, \mathcal{E}}$ for two (different but close) values of the energy, namely $\mathcal{E}^{(P_1)}$ and $\mathcal{E}^{(P_2)}$. More precisely, if we zoom the second panel of the second row (see Fig. 6) we easily realize that P_1 and P_2 are given, respectively, by an inner and outer tangency, justifying their unstable and stable nature. Moreover, we can see the fixed point A and B, which generalize the anti-aligned and aligned apsidal corotation family to the non-planar case. Observing again the second panel of the second row, we realize that, for a given value of the energy, namely $\mathcal{E}^{(A)}$, \mathcal{S}_{σ_0} and $\mathcal{C}_{\sigma_0, \mathcal{E}^{(A)}}$ have an outer tangency in the point A, being A a stable fixed point. However, if we continue to decrease the value of σ_0 (third frame on the top of Fig. 5, correspondent to $\sigma_0 = 5.93 \cdot 10^{-3}$), we realize that the fixed point A becomes unstable, since it is given by a new inner tangency between the sphere and the surface of the energy (see the third panel of the second row).

³See Eq. (16) and recall that $\Omega_3 - \Omega_2 = \pi$.

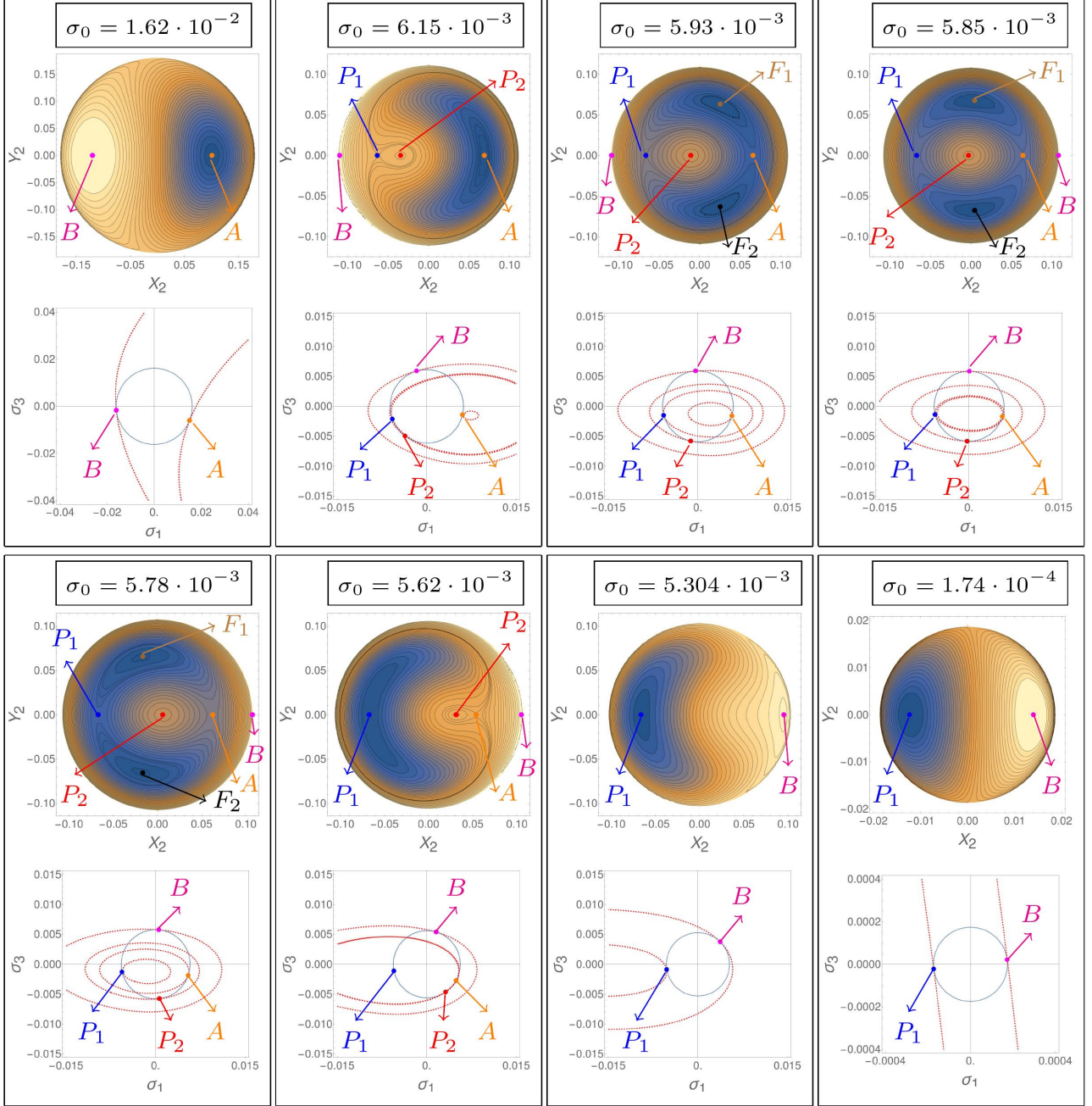


Figure 5: The first and third row show the contour plots already shown in Fig. 2, where the fixed points of the flow have been outlined with colored points and have been calculated through the tangency method explained in the text (i.e. solving Eqs. (26) and (27), together with the sphere condition (21), and expliciting the solutions in the Poincaré variables (X_2, Y_2) correspondently to the section $Y_3 = 0, \dot{Y}_3 \geq 0$). The values of σ_0 is fixed for each frame. Instead, in the second and fourth row there are reported the intersections of the sphere S_{σ_0} (represented in blue) and of the energy surfaces $C_{\sigma_0, \mathcal{E}}$ (red dashed curves) with the plane (σ_1, σ_3) for $\sigma_2 = 0$, for different values of the energy \mathcal{E} and values of σ_0 fixed as in the frame. The outlined points of tangency represent the CP1 points of the Hamiltonian flow (as outlined in the contour plot's above, in the same frame) and have been calculated by Eq. (26).

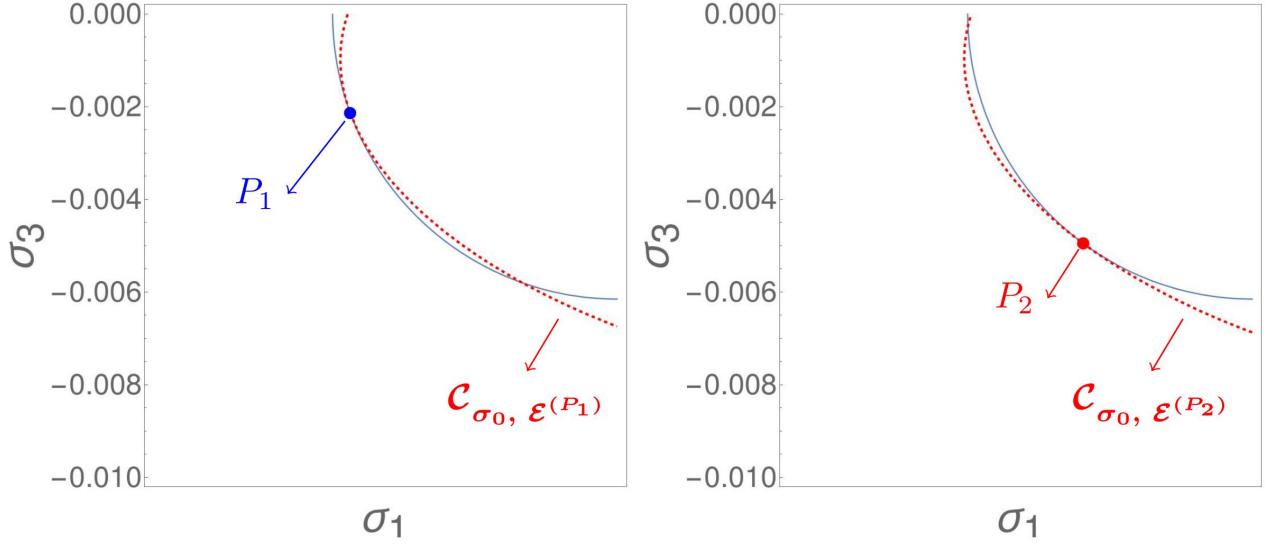


Figure 6: Zoom of the second panel of the second row of Fig. 5 (i.e. of the intersection between \mathcal{S}_{σ_0} and $\mathcal{C}_{\sigma_0, \mathcal{E}}$ with the plane (σ_1, σ_3) for $\sigma_2 = 0$ and $\sigma_0 = 6.15 \cdot 10^{-3}$). The blue and red points are, respectively, unstable and stable since they are given by an inner and outer tangency between \mathcal{S}_{σ_0} and $\mathcal{C}_{\sigma_0, \mathcal{E}}$. On the left we show the inner tangency between \mathcal{S}_{σ_0} and $\mathcal{C}_{\sigma_0, \mathcal{E}^{(P_1)}}$ in P_1 , while on the right the outer tangency between \mathcal{S}_{σ_0} and $\mathcal{C}_{\sigma_0, \mathcal{E}^{(P_2)}}$ in P_2 .

Roughly speaking we can say that, passing from the second to the third frame, i.e. decreasing the value of σ_0 from $\sigma_0 = 6.15 \cdot 10^{-3}$ to $\sigma_0 = 5.93 \cdot 10^{-3}$, the ellipsoid $\mathcal{C}_{\sigma_0, \mathcal{E}^{(A)}}$, initially external to the sphere \mathcal{S}_{σ_0} , decreases more and more, since it degenerates in a line tangent to the sphere (and the point of tangency satisfy both (26) and (27), together with the condition of the sphere (21), in the plane $\sigma_2 = 0$) and then it increases again, but now in the internal part of the sphere. Thus, the point A passes from stable to unstable by an inverse pitchfork bifurcation, which gives rise to two new stable fixed points, called F_1 and F_2 . They are not represented in the second and last row of Fig. 5 since they are CP2, i.e. they can be obtained solving (27), and they are out of the plane $\sigma_2 = 0$. They represent the points in which the ellipsoid $\mathcal{C}_{\sigma_0, \mathcal{E}}$ (that, recall, has cylindrical symmetry with respect to $\sigma_2 = 0$) pierces the sphere \mathcal{S}_{σ_0} . More precisely there exists an energy, namely, $\mathcal{E}^{(F)}$, for which the ellipsoid-like surface $\mathcal{C}_{\sigma_0, \mathcal{E}^{(F)}}$ is reduced to a line and pierces the sphere \mathcal{S}_{σ_0} in two points, called F_1 and F_2 , of coordinates $(\sigma_1^{(F)}, \sigma_2^{(F)}, \sigma_3^{(F)})$ and $(\sigma_1^{(F)}, -\sigma_2^{(F)}, \sigma_3^{(F)})$ (see the left plot of Fig. 7). Taking a larger value of the energy $\mathcal{E} > \mathcal{E}^{(F)}$, the radius of the ellipsoid-like surface is increased and the 3D cylinder intersects the sphere in two closed curves surrounding F_1 and F_2 . As an example we take $\mathcal{E} = \mathcal{E}_1^{(F)}$ be the energy of the black dotted curves represented in the third top panel of Fig. 5 and surrounding the F -modes. The surface $\mathcal{C}_{\sigma_0, \mathcal{E}_1^{(F)}}$ is represented in the central 3D plot of Fig. 7, while the plots on the right show the projection of the 3D plot in the plane $\sigma_2 = 0$.

Continuing to decrease the value of σ_0 (fourth top frame of Fig. 5) we observe that the point B passes from the negative to the positive semi-plane $X_2 \geq 0$. In fact, by the definition of the Hopf

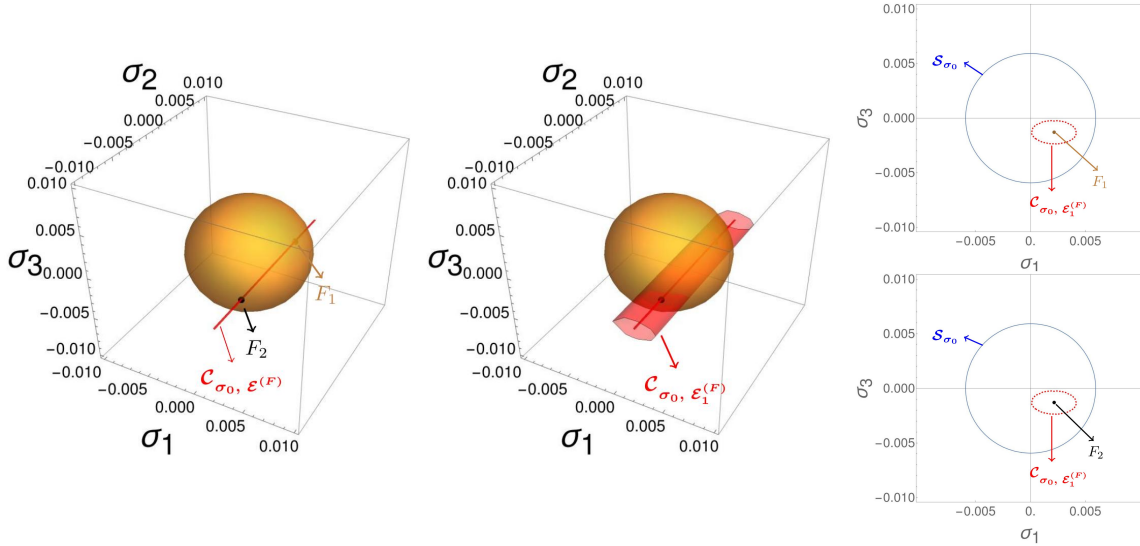


Figure 7: Graphical representation of the critical points of second type F_1 and F_2 in the case $\sigma_0 = 5.93 \cdot 10^{-3}$. Left: 3D representation of the sphere \mathcal{S}_{σ_0} and the surface $\mathcal{C}_{\sigma_0, \mathcal{E}^{(F)}}$, where $\mathcal{E}^{(F)}$ represents the energy of the fixed points F_1 and F_2 . We can observe that the surface of the energy pierces the sphere in the F -modes. Centre: As before, but in this case we plot also $\mathcal{C}_{\sigma_0, \mathcal{E}_1^{(F)}}$, where $\mathcal{E}_1^{(F)} > \mathcal{E}^{(F)}$ is the energy of the closed dotted curves surrounding the F -modes in the third upper plot of Fig. 5. In our numerical example $\mathcal{E}^{(F)} = -1.7366 \cdot 10^{-5}$ and $\mathcal{E}_1^{(F)} = -1.7362 \cdot 10^{-5}$. We can observe that $\mathcal{C}_{\sigma_0, \mathcal{E}_1^{(F)}}$ is an ellipsoid-like surface, with cylindrical symmetry, surrounding $\mathcal{C}_{\sigma_0, \mathcal{E}^{(F)}}$. Right: The projection of the 3D central plot in the plane $\sigma_2 = 0$.

variables (Eq. (18)) and of Poincaré variables (Eq. (15)), corresponding to the section $\omega_3 = \pi$ we are considering, $\sigma_1 = X_2 X_3$, where $X_3 \geq 0$. This means that when σ_1 becomes positive (as it does, as shown in the bottom Fig. of the fourth frame), the same holds for X_2 . Moreover, the fixed points F_1 and F_2 move initially away from the fixed point A while later, for still smaller value of σ_0 (see the first frame in the bottom row of Fig. 5, correspondent to $\sigma_0 = 5.78 \cdot 10^{-3}$), they approach the fixed point P_1 . Finally, decreasing again σ_0 , the fixed points F_1, F_2 collide with P_1 (see for instance the second frame, bottom row of Fig. 5, with $\sigma_0 = 5.62 \cdot 10^{-3}$). This terminates the F -family of periodic orbits, by an inverse pitchfork bifurcation which renders the point P_1 stable.⁴ In fact, passing from the first to the second panel of the bottom row of Fig. 5, we can observe the passage from an inner tangency between \mathcal{S}_{σ_0} and $\mathcal{C}_{\sigma_0, \mathcal{E}}$ in the point P_1 , to an outer tangency. This is not totally evident by the second panel of the bottom row, since the ellipse is so small to do not be visible, but it is noticeable in the third panel of the same row. Moreover, we can observe that the points P_2 and A become very close (look also at the ellipses tangent to the sphere in P_2 and A, represented in the second panel of the bottom row of Fig. 5, that seems quite overlapped) and, decreasing σ_0 , they disappear for an inverse saddle-node bifurcation. Thus, finally, the only stable points surviving to the chain of bifurcations are P_1 and B.

However, comparing Fig. 5 (or, equivalently, Fig. 4) with Fig. 1 we easily realize that the study of the integrable case does not represent correctly the real behaviour of the system. In fact the sequence

⁴This phenomena is equivalent, but inverse, to the same already described for the birth of the fixed point F_1 and F_2 from A, causing the passage of A from stable to unstable. The same inverse phenomena happens in this case.

of bifurcations obtained in the integrable approximation (\mathcal{H}_{int}) and in the full secular model (\mathcal{H}_{sec}) are not the same (see [12] for a more complete description of the sequence of bifurcations in the full secular model). For this reason, in the following Section we introduce a normal form so to arrive at a more accurate integrable approximation of the Hamiltonian model able to qualitatively describe the sequence of bifurcations shown in the secular complete Hamiltonian system.

3.3 The normalized integrable Hamiltonian

In this section we propose a normal form approach so to ‘enrich’ the integrable part of the Hamiltonian \mathcal{H}_{int} by terms that can be relevant for the qualitative representation of the chain of bifurcations of the complete system.

We start from the Hamiltonian written in Eq. (17), given by

$$\mathcal{H}_{sec}(\psi, \varphi, \Gamma, J) = \mathcal{H}_{int}(\psi, \Gamma; J) + \mathcal{H}_{1,space}(\psi, \varphi, \Gamma, J)$$

and we write \mathcal{H}_{int} as

$$\mathcal{H}_{int}(\psi, \Gamma; J) = Z_0(J) + \lambda Z_{0,1}(\psi, \Gamma; J),$$

where

$$Z_0(J) = c + \omega J \quad (28)$$

is the normal form term (with c a constant value) and λ is the book-keeping parameter, that is numerically equal to one, used in order to select the order of the terms to be normalized. With this notation, the Hamiltonian can be rewritten as

$$\mathcal{H}^{(0)} = \mathcal{H}_{sec}(\psi, \varphi, \Gamma, J) = Z_0(J) + \lambda Z_{0,1}(\psi, \Gamma; J) + \lambda \mathcal{H}_{1,space}(\psi, \varphi, \Gamma, J). \quad (29)$$

The aim is to find a generating function, namely χ , so to remove the dependence of $\mathcal{H}_{1,space}$ on the angle φ ; recalling that all the terms contained in $\mathcal{H}_{1,space}$ depend on the angle φ (while the terms independent on φ are collected in \mathcal{H}_{int}), this means solving the following homological equation:

$$\{Z_0, \chi\} + \lambda \mathcal{H}_{1,space} = 0. \quad (30)$$

After having found χ (*that is of order* $\mathcal{O}(\lambda)$), we can compute the normalized (after one-step) Hamiltonian

$$\mathcal{H}^{(1)} = \exp L_\chi \mathcal{H}^{(0)},$$

where $\exp L_\chi \cdot = \sum_{j \geq 0} (L_\chi^j \cdot) / j!$ is the Lie series operator, $L_\chi \cdot = \{\cdot, \chi\}$ is the Lie derivative with respect to the dynamical function χ and $\{\cdot, \cdot\}$ represents the Poisson bracket. A possible simple approximated normalized model that can be studied is the following: since $\mathcal{H}^{(0)}$ is of order $\mathcal{O}(\lambda)$, the first important correction is given by the contribution of order $\mathcal{O}(\lambda^2)$. Thus, we are interested in the integrable part of the normalized Hamiltonian of order 2 in the book-keeping λ . Recalling the homological equation (30), we observe that

$$\begin{aligned} \mathcal{H}^{(1)} &= \underbrace{Z_0 + \lambda Z_{0,1}}_{\mathcal{H}_{int}^{\mathcal{O}(\lambda)}} + \underbrace{\lambda \mathcal{H}_{1,space} + \{Z_0, \chi\}}_{=0} + \underbrace{\lambda \{Z_{0,1}, \chi\}}_{\mathcal{O}(\lambda^2)} + \underbrace{\lambda \{\mathcal{H}_{1,space}, \chi\} + \frac{1}{2} \{\{Z_0, \chi\}, \chi\}}_{=\frac{\lambda}{2} \{\mathcal{H}_{1,space}, \chi\}} + \mathcal{O}(\lambda^3) \\ &= \mathcal{H}_{int}^{(1)} + \mathcal{H}_{rest}^{(1)} + \mathcal{O}(\lambda^3) \end{aligned} \quad (31)$$

where⁵

$$\mathcal{H}_{int}^{(1)} = \mathcal{H}_{int} + \left(\frac{\lambda}{2} \{ \mathcal{H}_{1,space}, \chi \} \right) (\psi, \Gamma; J), \quad (32)$$

while the remaining part $\mathcal{H}_{rest}^{(1)}$ is made by⁶ $\{Z_{0,1}, \chi\}$ and all the terms of $\left(\frac{\lambda}{2}\{\mathcal{H}_{1,space}, \chi\}\right)$ depending on φ .

Before going on we have to make a couple of observations. First, from a practical point of view, it can be easier to perform the above normalization method in the variables (w_2, w_3, W_2, W_3) , introduced in Eq. (9), rather than $(\psi, \varphi, \Gamma, J)$; in fact, using the latter variables, there can appear, in the denominator, terms of the form $\sqrt{J^2 - \Gamma^2}$, leading to some simplifications problems for the calculator. For this reason, according to Eq. (16), we write the Hamiltonian given by Eq. (17) as

$$\mathcal{H}_{sec}(w_2, w_3, W_2, W_3) = \mathcal{H}_{int}(\psi, W_2, W_3) + \mathcal{H}_{1,space}(\psi, \varphi, W_2, W_3)$$

leaving implicit the dependence on w_2 and w_3 through $\psi = w_2 - w_3$, $\varphi = w_2 + w_3$, and we write \mathcal{H}_{int} as

$$\mathcal{H}_{int} = Z_0(W_2, W_3) + \lambda Z_{0,1}(\psi, W_2, W_3),$$

where

$$Z_0(W_2, W_3) = c + aW_2 + bW_3, \quad (33)$$

obtaining

$$\mathcal{H}^{(0)} = \mathcal{H}_{sec}(w_2, w_3, W_2, W_3) = Z_0(W_2, W_3) + \lambda Z_{0,1}(\psi, W_2, W_3) + \lambda \mathcal{H}_{1,space}(\psi, \varphi, W_2, W_3). \quad (34)$$

Thus, writing the Taylor-Fourier expansion of $\mathcal{H}_{1,space}$ as

$$\mathcal{H}_{1,space}(\psi, \varphi, W_2, W_3) = \sum_{l,m,n,k} \theta_{l,m,n,k} W_2^l W_3^m e^{in\psi} e^{ik\varphi} = \sum_{l,m,n,k} \theta_{l,m,n,k} W_2^l W_3^m e^{i((n+k)w_2 - (n-k)w_3)}$$

and recalling the homological equation (30), we obtain

$$\chi(\psi, \varphi, W_2, W_3) = \lambda \sum_{\substack{l,m,n,k \\ k \neq 0 \wedge \\ a(n+k) \neq b(n-k)}} \frac{\theta_{l,m,n,k}}{i(a(n+k) - b(n-k))} W_2^l W_3^m e^{in\psi} e^{ik\varphi}$$

and

$$\mathcal{H}_{int}^{(1)}(w_2 - w_3, W_2, W_3) = \mathcal{H}_{int} + \left(\frac{\lambda}{2} \{ \mathcal{H}_{1,space}, \chi \} \right) (\psi, W_2, W_3). \quad (35)$$

Finally, we have to remark the following: called ε the book-keeping parameter for the order in eccentricities and inclination, the initial model we take into account is the secular Hamiltonian approximation \mathcal{H}_{sec} truncated to the maximum book-keeping order N_{bk} (corresponding also to the maximum order of eccentricities appearing in \mathcal{H}_{sec}). Recalling that W_i is $\mathcal{O}(\varepsilon^2)$, in order to obtain the final normalized integrable Hamiltonian compatible with our initial model, we have to truncate $\mathcal{H}^{(1)}$ so to have maximum order of the eccentricities $\mathcal{O}(\varepsilon^{N_{bk}})$.

⁵With $\left(\frac{\lambda}{2}\{\mathcal{H}_{1,space}, \chi\}\right) (\psi, \Gamma; J)$ we refer to all the terms of $\frac{\lambda}{2}\{\mathcal{H}_{1,space}, \chi\}$ **not** depending on the angle φ .

⁶Since all the term contained by $\{Z_{0,1}, \chi\}$ depend on φ , it does not contribute to the integrable part of the normalized Hamiltonian $\mathcal{H}_{int}^{(1)}$, but only to the remaining part $\mathcal{H}_{rest}^{(1)}$.

3.3.1 Phase space and geometrical analysis of the fixed points of the integrable normalized Hamiltonian

Starting from the normalized integrable Hamiltonian $\mathcal{H}_{int}^{(1)}$ described in the previous section (see Eq. (35)), we can proceed analogously to Section 3.2.2, i.e. we compute the Poincaré surface of section and analyze the corresponding phase space and periodic orbits using the Hopf variables.

Using the change of variables (16) and (15), the Poincaré surface of section $\mathcal{P}_{int}^{(1)}(\mathcal{E}; \text{AMD})$, at a fixed level of energy \mathcal{E} , is defined by

$$\mathcal{P}_{int}^{(1)}(\mathcal{E}; \text{AMD}) = \left\{ (X_2, Y_2, X_3, Y_3) \in \mathbb{R}^4 : \mathcal{H}_{int}^{(1)}(X_2, Y_2, X_3, Y_3 = 0; \text{AMD}) = \mathcal{E}, Y_3 = 0, \right. \\ \left. \dot{Y}_3 = -\frac{\partial \mathcal{H}_{int}^{(1)}}{\partial X_3} \Big|_{Y_3=0} \geq 0, \cos(i_{max}) \leq \cos(i_{mut})(X_2, Y_2, X_3, Y_3 = 0; \text{AMD}) \leq 1 \right\}.$$

They are shown in Fig. 8 for different (increasing, from left to right, from top to bottom) levels of energy. Some comments immediately arise.

First of all, we can see that the sequence of bifurcations produced in the former case is different with respect to the ones of the integrable case (see Fig. 2); the difference will appear much more evident analysing the phase space in the Hopf variables (see the description in the following). Instead, we can observe a similarity with the Poincaré surface of section of the full secular Hamiltonian \mathcal{H}_{sec} (see Fig. 1). Obviously, we can compare the sequence of bifurcations produced by the integrable normalized model ($\mathcal{P}_{int}^{(1)}(\mathcal{E}; \text{AMD})$) by that of the full secular case ($\mathcal{P}_{sec}(\mathcal{E}; \text{AMD})$) only for values of the energy for which we are in the *nearly-planar regime*. More precisely, in the full secular case, we know that there exists a critical value of the energy, namely \mathcal{E}_C , for which a saddle-node bifurcation occurs, giving rise to two fixed points of the Poincaré map, corresponding to periodic orbits called the Kozai–Lidov orbits (see [12]). We call *transition regime*⁷ the one holding at energies in the interval $\mathcal{E}_C \leq \mathcal{E} \leq \mathcal{E}_{C,2}$. For values of the energy $\mathcal{E} > \mathcal{E}_{C,2}$ we are in the *Kozai-Lidov regime*, characterized by the transition of one of this point from stable to unstable (see, for example, the last two panels of Fig. 1). It is evident that such a transition cannot be observed in the integrable normalized Hamiltonian model, where we do not consider the terms giving birth to the Kozai-Lidov mechanism. Thus, the sequence of bifurcations shown in the last row of Fig. 8 cannot be representative of the full secular model. Moreover, also when the sequence of bifurcations between the normalized integrable case and the full secular one seem to be the same, some difference arise in the topology. For example, comparing the third panel in the top row of Fig. 8 with the second panel of Fig. 1, we can notice that, in the first case, the saddle node bifurcation occurs in a more inner region with respect to the second case, where the fixed point appears to be very close to the curve delimiting the regions dominated by the apsidal corotations. However, despite some differences in the topology, the new normalized integrable Hamiltonian model, contrary to the simple integrable one, is able to represent correctly the ‘real’ sequence of bifurcations.

As in the integrable case, we want to analyze, using the Hopf variables, the phase space and the sequence of bifurcation, outlining also the difference with the integrable case. First of all, as already done in section 3.2.1, we determine the phase portraits for $\mathcal{H}_{int}^{(1)}(\sigma_1, \sigma_3; \sigma_0)$ at a fixed level of σ_0 , for different (decreasing) values of σ_0 . In the first row of Figs. 9a, 9b, 9c are reported the contour plots of $\mathcal{H}_{int}^{(1)}(X_2, Y_2; \sigma_0)$, correspondent to the section $Y_3 = 0, \dot{Y}_3 \geq 0$. We notice that the produced plots give rise to the same sequence of bifurcations shown in the (numerical) Poincaré surface of sections,

⁷Between the nearly-planar regime and the Kozai-Lidov one.

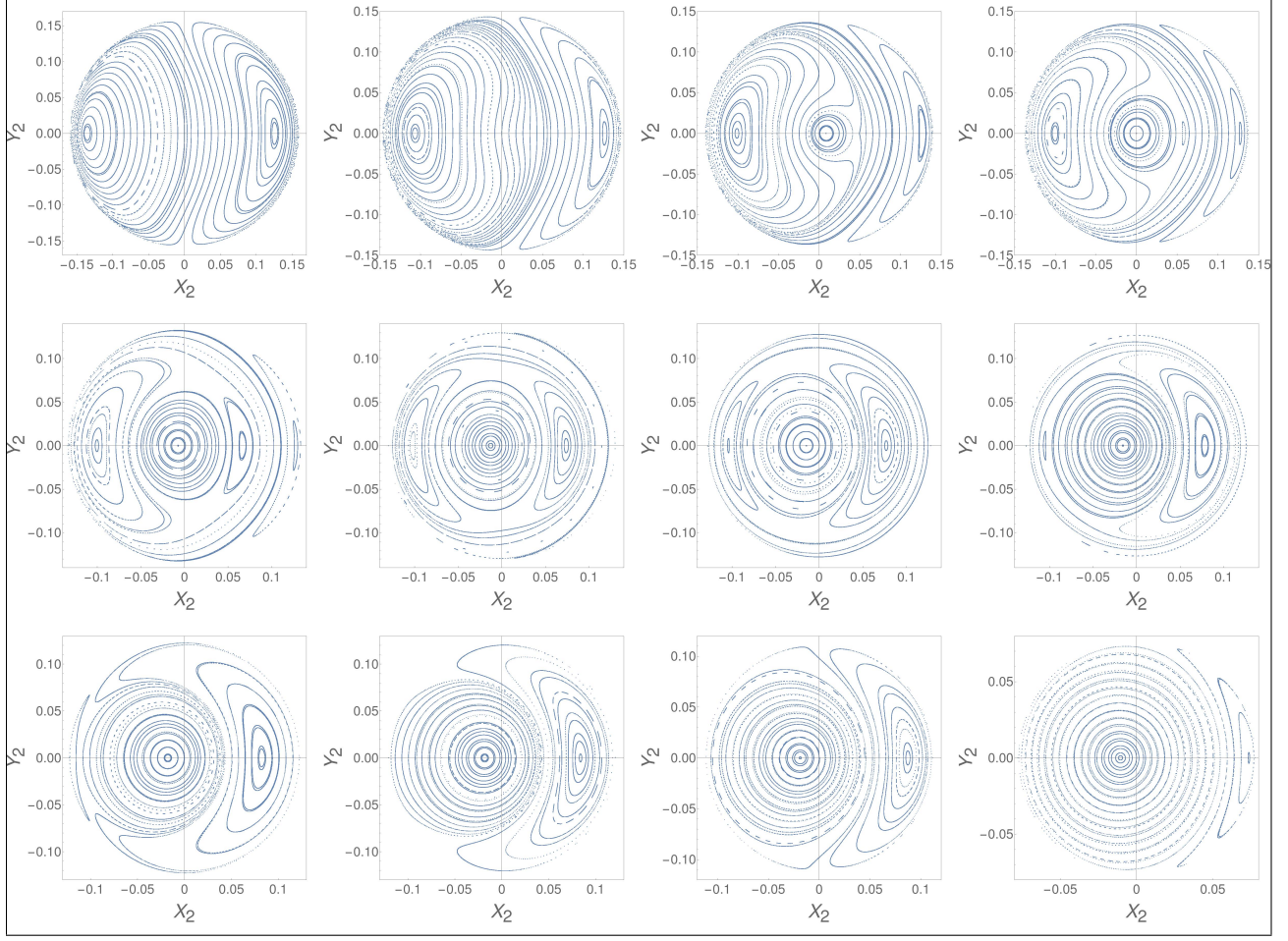


Figure 8: Poincaré surfaces of section $\mathcal{P}_{int}^{(1)}(\mathcal{E}; \text{AMD})$ in the plane (X_2, Y_2) with L_z fixed and different values of energy. The surfaces of section are computed by a numerical integration of trajectories of the normalized integrable Hamiltonian $\mathcal{H}_{int}^{(1)}$ (Eq. (35)) truncated at multipolar degree $N_P = 5$, order $N_{bk} = 12$ in the eccentricities, and energies (from top to bottom, from left to right) $\mathcal{E} = -5.82 \cdot 10^{-5}, -4.3 \cdot 10^{-5}, -3.59 \cdot 10^{-5}, -3.34 \cdot 10^{-5}, -3.03 \cdot 10^{-5}, -2.68 \cdot 10^{-5}, -2.51 \cdot 10^{-5}, -2.42 \cdot 10^{-5}, -2.12 \cdot 10^{-5}, -1.99 \cdot 10^{-5}, -1.44 \cdot 10^{-5}, -3.3 \cdot 10^{-6}$. In this case the values of the energy for which we can have co-planar orbits are $\mathcal{E}_{min} = -1.71 \cdot 10^{-4}$ and $\mathcal{E}_{2,3} = -5.82 \cdot 10^{-5}$. We start consider values of energy $\mathcal{E} \geq \mathcal{E}_{2,3}$ for which the Poincaré sections are complete.

represented in Fig. 8. Moreover, we observe that, up to terms of second order in the variables σ_i (i.e. of fourth order in the eccentricities), we find

$$\mathcal{H}_{int}^{(1)} = A\sigma_1^2 + C\sigma_3^2 + B\sigma_1\sigma_3 + D(\sigma_0)\sigma_1 + E(\sigma_0)\sigma_3 + F(\sigma_0)$$

where A, B, C are constants, while the functions $D(\sigma_0)$ and $E(\sigma_0)$ are linear in σ_0 and $F(\sigma_0)$ contains

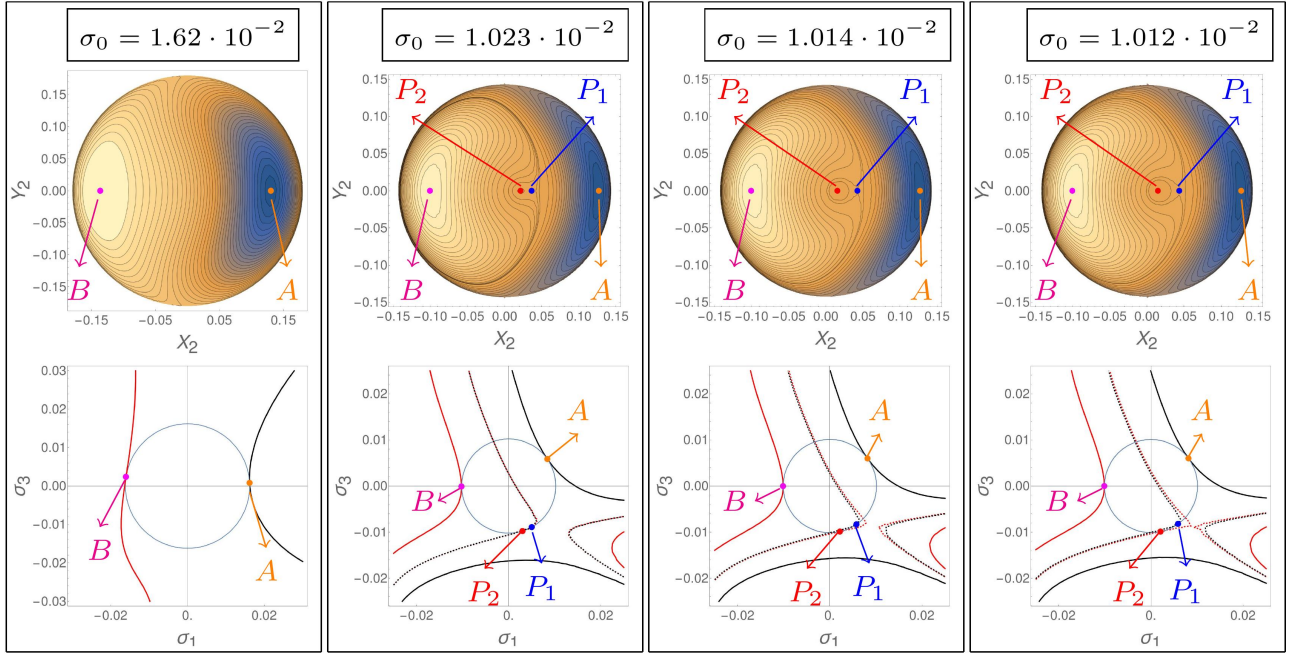
terms linear and quadratic in σ_0 . In our numerical example the coefficients of $\mathcal{H}_{int}^{(1)}$ are given by:

$$\begin{aligned} A &= 0.00912208, & C &= -0.0518887, \\ B &= 0.00782589, & D(\sigma_0) &= 0.000425947 + 0.00634477 \sigma_0, \\ E(\sigma_0) &= 0.00101564 - 0.118017 \sigma_0, & F(\sigma_0) &= -0.0011129 \sigma_0 - 0.164326 \sigma_0^2. \end{aligned}$$

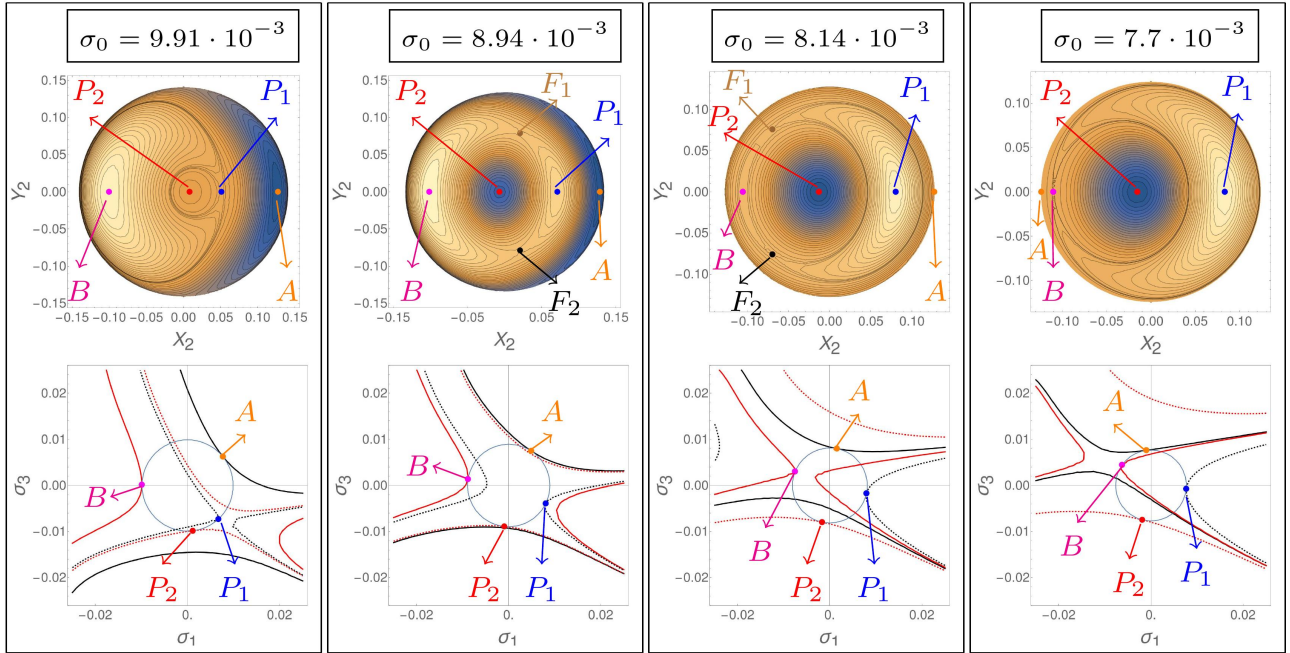
Contrary to the simple integrable case, the quadratic form $A\sigma_1^2 + C\sigma_3^2 + B\sigma_1\sigma_3^2$ yields hyperbola, being A, B, C such that $B^2 > 4AC$. Thus, for any permissible value \mathcal{E} , the surface $\mathcal{C}_{\sigma_0, \mathcal{E}}$ intersects the plane $\sigma_2 = 0$ along local hyperbola-like curves (see the second row of Figs. 9a, 9b, 9c). This causes a remarkable difference between the nature of the bifurcations obtained in the integrable normalized case and in the integrable one.

We can now analyze the sequence of bifurcations in the normalized integrable case; it is shown in Fig. 9. In the first frame of Fig. 9a we can see the apsidal corotation orbits. Analogously to the integrable case, we find that \mathcal{S}_{σ_0} and $\mathcal{C}_{\sigma_0, \mathcal{E}}$ (where $\sigma_0 = \sigma_{0max} = 1.62 \cdot 10^{-2}$) have two tangency points, called A and B, respectively for $\mathcal{E} = \mathcal{E}_{min}$ and $\mathcal{E} = \mathcal{E}_{2,3}$ (see caption of Fig. 8). Thus, the associated orbits yield two coplanar ellipses with, respectively, anti-aligned and aligned pericenters precessing by the same frequency. Decreasing the value of σ_0 (second frame of Fig. 9a), we can observe that a *saddle-node* bifurcation takes place, giving rise to two new fixed points of the Poincaré map, corresponding to periodic orbits called P_1 and P_2 . We note that this type of bifurcation is inverted with respect to the integrable case (see the second panel of Fig. 5). They are given (second frame of Fig. 9a, bottom panel), respectively, by an inner/outer tangency between the sphere \mathcal{S}_{σ_0} and the energy surfaces $\mathcal{C}_{\sigma_0, \mathcal{E}}$ for two (not equal but close) values of the energy, namely $\mathcal{E}^{(P_1)}$ and $\mathcal{E}^{(P_2)}$. The zoomed plot is shown in Fig. 10. Thus, the point P_1 is unstable, while P_2 is stable.

If we continue to decrease the value of σ_0 (look at the passage between the top panels of the second, third and last frame of Fig. 9a) we realize that the area of the region surrounding the stable point P_2 grows. Correspondingly, the hyperbola having the tangency point with the sphere in P_1 (black dotted) and P_2 (red dotted) (bottom panels of the second, third and last frame of Fig. 9a) become further away. It is interesting to observe that, in such a sequence of plots, the branches of the hyperbola tangent to the sphere in P_2 get closer and closer, until, furthermore decreasing the value of σ_0 , the branches touch each other and the hyperbola change its direction (see the first bottom panel of Fig. 9b). We note that, in all the previous described pictures, the apsidal corotations A and B always appear, maintaining their stable nature. We can now analyze the second frame of Fig. 9b; we note that, apart the apsidal corotations A and B and the stable point P_2 , the top panel is characterized by the stable character of P_1 and the birth of other two fixed points. More precisely, passing from the first to the second top panel of Fig. 9b, we can see that the fixed point P_1 passes from unstable to stable by a pitchfork bifurcation, giving rise to two new *unstable* fixed points F_1 and F_2 . In fact, as outlined by the correspondent bottom panels, we can see that, while in the first bottom panel P_1 represents the inner tangency point between a branch of the black dotted hyperbola and the sphere, instead in the second bottom panel it is given by the outer tangency between the other branch of a new hyperbola (i.e., of a new surface of energy) and the sphere. Concerning the F points, as in the integrable case, they are critical points of the second kind. Thus, they are not in the plane $\sigma_2 = 0$ and they represent the points in which the hyperbola-like surface $\mathcal{C}_{\sigma_0, \mathcal{E}}$ (having cylindrical symmetry with respect to $\sigma_2 = 0$) pierces the sphere \mathcal{S}_{σ_0} (see Fig. 11). More precisely, it can be seen that there exist a value of the energy, namely $\mathcal{E}^{(F)}$, for which the hyperbola “degenerates” in the union of two planes (i.e. the two branches of the hyperbola touch each other) and their intersection creates a line, piercing



(a)

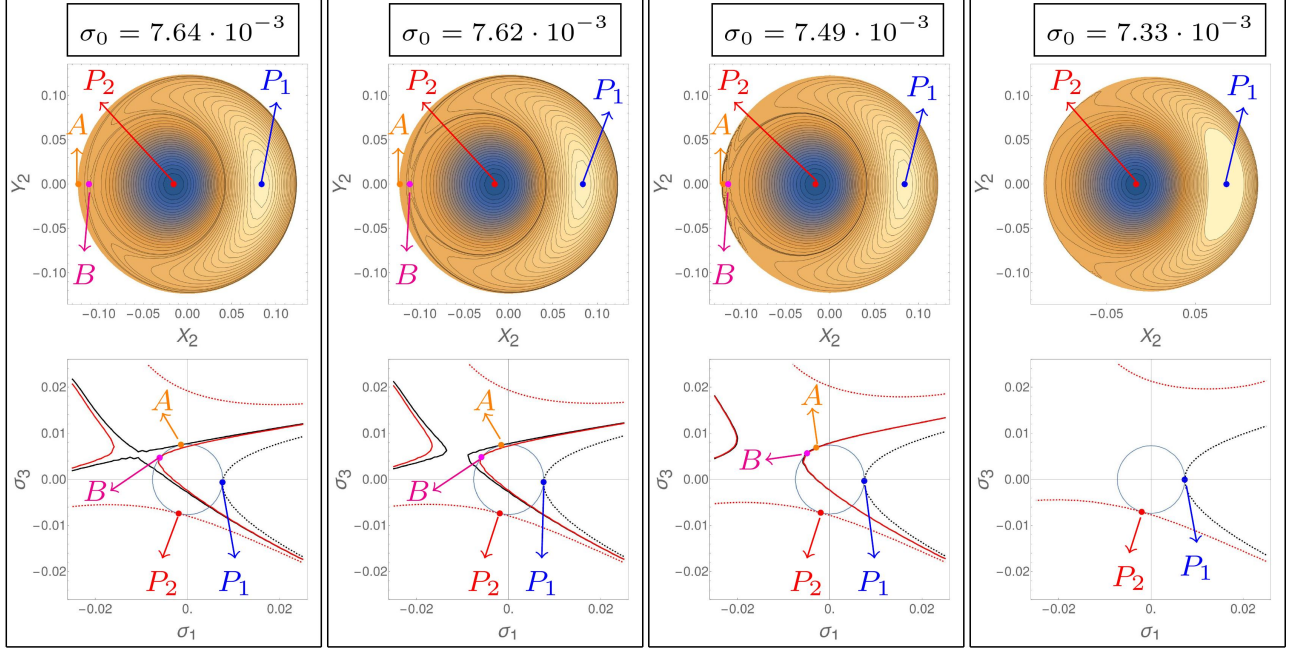


(b)

Figure 9

the sphere in the points F_1 and F_2 ⁸. For still smaller value of σ_0 (see the third frame of Fig. 9b) the

⁸This will be clearer in Section 4.2.2, where we will find the precise value of σ_0 for which the CP1 and CP2 occur.



(c)

Figure 9: The first rows of Figs. 9a, 9b, and 9c show the contour plots, correspondent to $Y_3 = 0$, $\dot{Y}_3 \geq 0$, of $\mathcal{H}_{int}^{(1)}(X_2, Y_2; \sigma_0) = \mathcal{E}$ in the plane (X_2, Y_2) , with Hamiltonian \mathcal{H} truncated at multipolar degree $N_P = 5$, at order $N_{bk} = 12$ in the eccentricities, and decreasing values of σ_0 (as explicitly indicated in the top of each frames). The fixed points of the flow have been outlined with colored points and have been calculated through the tangency method explained in the text (i.e. solving Eqs. (26) and (27), together with the sphere condition (21), and expliciting the solutions in the Poincaré variables (X_2, Y_2) correspondingly to the section $Y_3 = 0$, $\dot{Y}_3 \geq 0$). Instead, in the second rows of Figs. 9a, 9b, and 9c there are reported the intersections of the sphere \mathcal{S}_{σ_0} (represented in blue) and of the energy surfaces $\mathcal{C}_{\sigma_0, \mathcal{E}}$ with the plane (σ_1, σ_3) for $\sigma_2 = 0$, for different values of the energy \mathcal{E} and values of σ_0 fixed as in the frame. The outlined points of tangency represent the CP1 points of the normalized integrable Hamiltonian flow (as outlined in the countour plots above, in the same frame) and they have been calculated by Eq. (26). In this case, $\mathcal{C}_{\sigma_0, \mathcal{E}}$ has been represented by a continued/dashed red/black curve, depending on the tangency point. This choice has been done in order to outline the local hyperbola-like behaviour of the energy surface.

fixed points F_1 and F_2 move away from the fixed point of the orbit P_1 while later, for still smaller value of σ_0 (fourth frame of Fig. 9b), they collide with the B mode. This terminates the F -family of periodic orbits, by an inverse pitchfork bifurcations, rendering the point B unstable.

In fact, passing from the third to the fourth panel of the bottom row of Fig. 9b, we can observe the passage from an outer tangency between \mathcal{S}_{σ_0} and (the left red branch of) $\mathcal{C}_{\sigma_0, \mathcal{E}}$ in the point B (with $\sigma_0 = 8.14 \cdot 10^{-3}$), to an inner tangency (with the right red branch of $\mathcal{C}_{\sigma_0, \mathcal{E}}$ with $\sigma_0 = 7.7 \cdot 10^{-3}$ and a different value of the energy). Finally, in the same frame, we observe also the passage of A from the positive to the negative semi-plane $X_2 \leq 0$, as, correspondingly, σ_1 does. Finally, continuing to decrease the value of σ_0 (look at the first frame of Fig. 9c) we see that the modes A and B become closer and closer; in particular, looking at the bottom panel of the same frame, we realize that the more σ_0 is decreased, the closer are the branches of the black hyperbola (tangent to the sphere in the point A), until the hyperbola changes its orientation (see the second bottom panel of Fig. 9c).

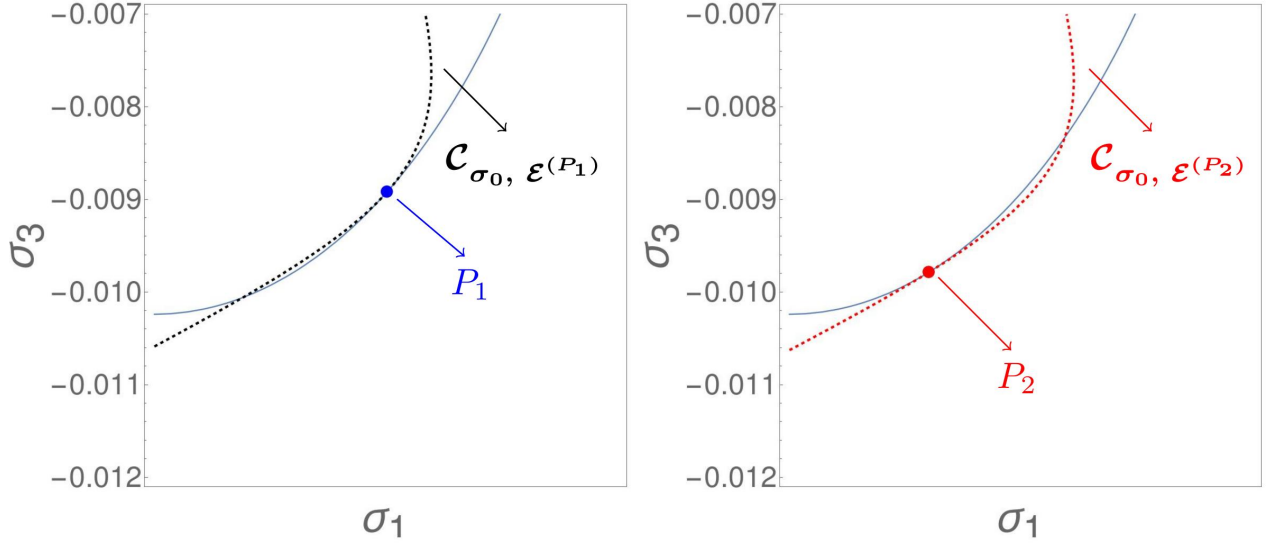


Figure 10: Zoom of the second plot of the second row of Fig. 9a (i.e. of the intersection between \mathcal{S}_{σ_0} and $\mathcal{C}_{\sigma_0, \mathcal{E}}$ with the plane (σ_1, σ_3) for $\sigma_2 = 0$ and $\sigma_0 = 1.023 \cdot 10^{-2}$). The blue and red points are, respectively, unstable and stable since they are given by an inner and outer tangency between \mathcal{S}_{σ_0} and $\mathcal{C}_{\sigma_0, \mathcal{E}}$. On the left we show the inner tangency between \mathcal{S}_{σ_0} and $\mathcal{C}_{\sigma_0, \mathcal{E}^{(P_1)}}$ in P_1 , while on the right the outer tangency between \mathcal{S}_{σ_0} and $\mathcal{C}_{\sigma_0, \mathcal{E}^{(P_2)}}$ in P_2 (in our example $\mathcal{E}^{(P_1)} = -3.78701$ and $\mathcal{E}^{(P_2)} = -3.78861$).

Finally, correspondingly to the third frame of Fig. 9c, the hyperbolas tangent to the sphere in the point A (black) and B (red) become so close that the points A and B collapse one on the other and, for a smaller value of σ_0 (look at the final frame of Fig. 9c), they disappear for an inverse saddle-node bifurcation. Thus, finally, the only stable points surviving to the chain of bifurcations are P_2 and P_1 .

4 Low-order approximation of the Hamiltonian

In the following section we want to analyze the sequence of bifurcations produced by Hamiltonian models obtained by considering lower multipolar order N_P and lower order of the eccentricity N_{bk} . In this way, we would like to understand if it exists a simpler integrable Hamiltonian approximation able to qualitatively describe the same sequence of bifurcations of the secular Hamiltonian approximation \mathcal{H}_{sec} , obtained considering $N_P = 5$, $N_{bk} = 12$ and shown in Fig. 1. A similar question has been answered in [12], analyzing the sequence of bifurcations in the case $N_P = 4$, $N_{bk} = 10$ (see Fig. 6 of that article). Moreover, we want to determine analytical equations allowing to find the precise values of σ_0 for which critical points of the first and second kind occur. Thus, the objective of the following Section is to derive the *bifurcation value* of σ_0 for a generic Hamiltonian \mathcal{K}_I introduced in Eq. (36).

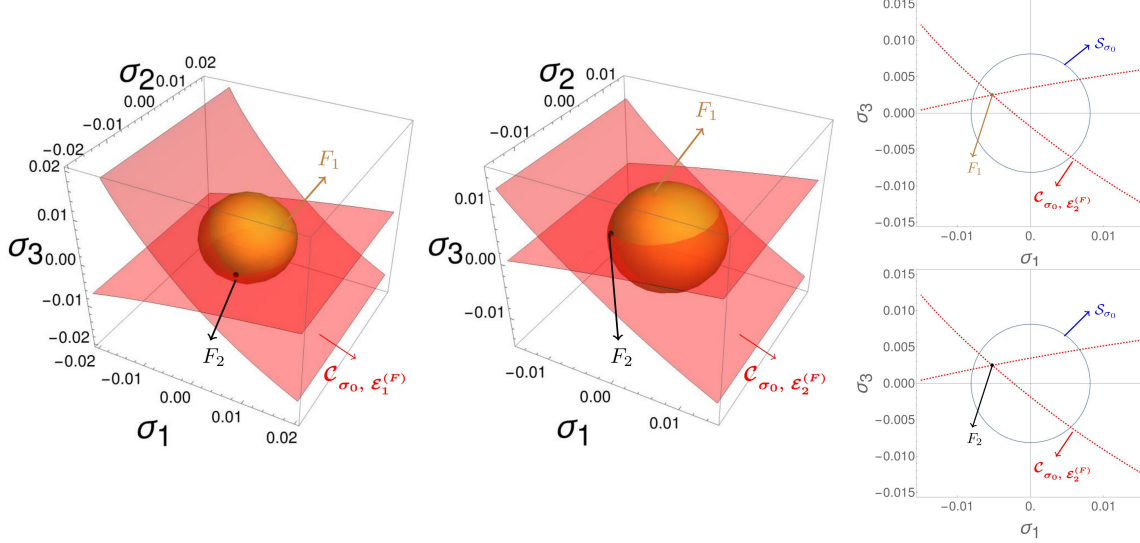


Figure 11: Graphical representation of the critical points of second kind F_1 and F_2 . Left: 3D representation of the sphere \mathcal{S}_{σ_0} and the surface $\mathcal{C}_{\sigma_0, \mathcal{E}_1^{(F)}}$, in the case $\sigma_0 = 8.94 \cdot 10^{-3}$, where $\mathcal{E}_1^{(F)}$ represents the energy of the fixed points F_1 and F_2 . We can observe that the surface of the energy pierces the sphere in the F -modes. Centre: As before, but in the case $\sigma_0 = 8.14 \cdot 10^{-3}$. For a value of the energy, namely $\mathcal{E}_2^{(F)}$, $\mathcal{C}_{\sigma_0, \mathcal{E}_2^{(F)}}$ pierces the sphere \mathcal{S}_{σ_0} in the points F_1 and F_2 of coordinates, respectively, $(\sigma_1^{(F)}, \sigma_2^{(F)}, \sigma_3^{(F)})$ and $(\sigma_1^{(F)}, -\sigma_2^{(F)}, \sigma_3^{(F)})$. Right: The projection of the 3D central plot (case $\sigma_0 = 8.14 \cdot 10^{-3}$) in the planes $\sigma_2 = 0$.

4.1 Contacts and bifurcations

Let us suppose to have a Hamiltonian \mathcal{K}_I , described in terms of the Hopf variables by:

$$\mathcal{K}_I(\sigma_1, \sigma_3; \sigma_0) = \mathcal{A}\sigma_1^2 + \mathcal{C}\sigma_3^2 + \mathcal{B}\sigma_1\sigma_3 + (\mathcal{D}_1\sigma_0 + \Delta_1)\sigma_1 + (\mathcal{D}_3\sigma_0 + \Delta_3)\sigma_3 \quad (36)$$

with $\mathcal{A}, \mathcal{B}, \mathcal{C}, \mathcal{D}_1, \mathcal{D}_3, \Delta_1, \Delta_3$ control parameters. Without loss of generality, through a rotation, we can set $\mathcal{B} = 0$. To find the non-degenerate critical points of Hamiltonian (36) we solve the equation (25), with the assumption that $(\mathcal{D}_1\sigma_0 + \Delta_1)$ and $(\mathcal{D}_3\sigma_0 + \Delta_3)$ are not both vanishing. This gives

$$\begin{aligned} \sigma_1^{(CP1)}(\mu, \sigma_0) &= -\frac{2(\mathcal{C} - \mu)(\mathcal{D}_1\sigma_0 + \Delta_1)}{4\mu^2 - 4(\mathcal{A} + \mathcal{C})\mu + 4\mathcal{A}\mathcal{C}}, \\ \sigma_2^{(CP1)}(\mu, \sigma_0) &= 0, \\ \sigma_3^{(CP1)}(\mu, \sigma_0) &= -\frac{2(\mathcal{A} - \mu)(\mathcal{D}_3\sigma_0 + \Delta_3)}{4\mu^2 - 4(\mathcal{A} + \mathcal{C})\mu + 4\mathcal{A}\mathcal{C}}. \end{aligned} \quad (37)$$

For the CP1, implementing the constraint

$$\mathcal{S}(\mu, \sigma_0) = (\sigma_1^{(CP1)}(\mu, \sigma_0))^2 + (\sigma_3^{(CP1)}(\mu, \sigma_0))^2 - \sigma_0^2 = 0,$$

we can look for the conditions to have more than two solutions (in μ) as an effect of changing σ_0 [6]. The numerator of $\mathcal{S}(\mu, \sigma_0) = 0$ corresponds to an equation of 4th degree in μ , namely

$$4(\mathcal{A} - \mu)^2(\mathcal{C} - \mu)^2 - (\mathcal{A} - \mu)^2 \mathcal{T}_3(\sigma_0) - (\mathcal{C} - \mu)^2 \mathcal{T}_1(\sigma_0) = 0, \quad (38)$$

where

$$\mathcal{T}_1(\sigma_0) = \left(\mathcal{D}_1 + \frac{\Delta_1}{\sigma_0} \right)^2, \quad \mathcal{T}_3(\sigma_0) = \left(\mathcal{D}_3 + \frac{\Delta_3}{\sigma_0} \right)^2.$$

When the number of real solutions of the above equation changes, we have the corresponding *bifurcation value* of σ_0 . The discriminant of (38) w.r.t. μ is a function in σ_0 whose simple zeros provide the required change in the number of solutions. It is given by

$$\begin{aligned} \mathcal{Q}(\sigma_0) = 64(\mathcal{A} - \mathcal{C})^2 \mathcal{T}_1(\sigma_0) \mathcal{T}_3(\sigma_0) & \left[(4(\mathcal{A} - \mathcal{C})^2 - \mathcal{T}_1(\sigma_0))^3 - 3\mathcal{T}_3(\sigma_0) \left(16(\mathcal{A} - \mathcal{C})^4 \right. \right. \\ & \left. \left. + 28\mathcal{T}_1(\sigma_0)(\mathcal{A} - \mathcal{C})^2 + \mathcal{T}_1(\sigma_0)^2 \right) + 3\mathcal{T}_3(\sigma_0)^2 (4(\mathcal{A} - \mathcal{C})^2 - \mathcal{T}_1(\sigma_0)) - \mathcal{T}_3(\sigma_0)^3 \right] \end{aligned} \quad (39)$$

Notice that $\mathcal{T}_1(\sigma_0) = 0$ or $\mathcal{T}_3(\sigma_0) = 0$ do not correspond to a change in the sign of the discriminant. At $\mathcal{A} = \mathcal{C}$ the discriminant is identically zero for every value of σ_0 ; this is the situation at which the ellipses degenerate to circles. Therefore, tangencies with the phase space can occur either at an infinite number of points or at no point. Higher order normal forms would be needed to describe the bifurcations. We do not consider this case here. By solving $\mathcal{Q}(\sigma_0) = 0$ with respect to $\mathcal{T}_3(\sigma_0)$ and considering the only real solution, the bifurcation values of σ_0 can be found by imposing

$$f_1(\sigma_0) = 0$$

where

$$f_1(\sigma_0) = -4(\mathcal{A} - \mathcal{C})^2 + \mathcal{T}_1(\sigma_0) + \mathcal{T}_3(\sigma_0) - 2^{2/3} 3 \left((\mathcal{A} - \mathcal{C})^2 \mathcal{T}_1(\sigma_0)^2 \right)^{1/3} + 2^{1/3} 6 \left((\mathcal{A} - \mathcal{C})^4 \mathcal{T}_1(\sigma_0) \right)^{1/3}. \quad (40)$$

Instead, the *bifurcation values* of σ_0 related to CP2 occur for values of σ_0 solving

$$f_2(\sigma_0) = -4 + \frac{\mathcal{T}_1(\sigma_0)}{\mathcal{A}^2} + \frac{\mathcal{T}_3(\sigma_0)}{\mathcal{C}^2} = 0.$$

The solution can be explicitly found:

$$\begin{aligned} \sigma_0^{(CP2,1)} &= -\frac{\mathcal{C}^2 \mathcal{D}_1 \Delta_1 + \mathcal{A}^2 \mathcal{D}_3 \Delta_3 + \mathcal{A} \mathcal{C} \sqrt{4\mathcal{C}^2 \Delta_1^2 - (\mathcal{D}_3 \Delta_1 + 2\mathcal{A} \Delta_3 - \mathcal{D}_1 \Delta_3)(\mathcal{D}_3 \Delta_1 - (2\mathcal{A} + \mathcal{D}_1) \Delta_3)}}{\mathcal{C}^2 \mathcal{D}_1^2 + \mathcal{A}^2 (-4\mathcal{C}^2 + \mathcal{D}_3^2)}, \\ \sigma_0^{(CP2,2)} &= -\frac{\mathcal{C}^2 \mathcal{D}_1 \Delta_1 + \mathcal{A}^2 \mathcal{D}_3 \Delta_3 - \mathcal{A} \mathcal{C} \sqrt{4\mathcal{C}^2 \Delta_1^2 - (\mathcal{D}_3 \Delta_1 + 2\mathcal{A} \Delta_3 - \mathcal{D}_1 \Delta_3)(\mathcal{D}_3 \Delta_1 - (2\mathcal{A} + \mathcal{D}_1) \Delta_3)}}{\mathcal{C}^2 \mathcal{D}_1^2 + \mathcal{A}^2 (-4\mathcal{C}^2 + \mathcal{D}_3^2)}. \end{aligned} \quad (41)$$

Geometrically, the appearance of the CP2 is due to the centers of the ellipses or hyperbolas entering or leaving the circle $\sigma_1^2 + \sigma_3^2 = \sigma_0^2$ (on the plane $\sigma_2 = 0$).

4.2 Octupolar approximation order of the Hamiltonian

The first non-integral approximation of the Hamiltonian is given by the *octupolar* approximation, i.e. $N_P = 3$. In fact, the quadrupolar approximation of the Hamiltonian, i.e. $N_P = 2$, is already integrable for the ‘‘happy coincidence’’ (see [10] or [14] for a review), corresponding to the non dependency of the Hamiltonian on the argument of the pericenter of the outer planet ω_3 . Moreover, the first non-trivial order of eccentricity is $N_{bk} = 4$. In fact in the case $N_{bk} = 2$ the Hamiltonian is a first order function

in the variables $(\sigma_0, \sigma_1, \sigma_3)$ (i.e. a plane). Thus, it can be proved that there exist at most two CPs of the first kind, while it is not possible to find physical meaningful CPs of the second kind. Thus, the easiest not-integrable Hamiltonian approximation that we can consider for our analysis is the one with $N_P = 3$ and $N_{bk} = 4$.⁹

4.2.1 Integrable octupolar approximation

First of all, we observe that the integrable approximation of the Hamiltonian obtained in closed form with $N_P = 3$ and $N_{bk} = 4$ is a quadratic polynomial in the Hopf variables of the form

$$\mathcal{H}_{int}^{(N_P=3, N_{bk}=4)} = A\sigma_1^2 + C\sigma_3^2 + B\sigma_1\sigma_3 + D(\sigma_0)\sigma_1 + E(\sigma_0)\sigma_3 + F(\sigma_0) \quad (42)$$

where A, B, C are constants, while the functions $D(\sigma_0)$ and $E(\sigma_0)$ are linear in σ_0 and $F(\sigma_0)$ contains terms linear and quadratic in σ_0 . In our numerical example the coefficients are given by:

$$\begin{aligned} A &= 0, & C &= 0.00871943, \\ B &= 0.00955933, & D(\sigma_0) &= 0.000554664 - 0.095445\sigma_0, \\ E(\sigma_0) &= 0.00006606 + 0.00168926\sigma_0, & F(\sigma_0) &= -0.001703\sigma_0 - 0.178404\sigma_0^2. \end{aligned}$$

The quadratic form $A\sigma_1^2 + C\sigma_3^2 + B\sigma_1\sigma_3$ yields obviously hyperbola, being $A = 0$ and then $B^2 > 4AC = 0$. We want to stress that, the octupolar approximation never produces terms of the form $\cos(2\omega_2 - 2\omega_3)$ and this is the reason for which we have no dependence on σ_1^2 , resulting $A = 0$. The first multipolar approximation producing dependence on σ_1^2 is $N_P = 4$. Thus, for any permissible value \mathcal{E} , the surface $\mathcal{C}_{\sigma_0, \mathcal{E}}$ intersects the plane $\sigma_2 = 0$ along hyperbola-like curves. However, analyzing the Poincaré surface of section $\mathcal{P}_{int}^{(N_P=3, N_{bk}=4)}(\mathcal{E}; \text{AMD})$, i.e. at a fixed level of energy and considering $\mathcal{H}_{int}^{(N_P=3, N_{bk}=4)}$ described in (42), we can notice that the described sequence of bifurcation is not the same as for the complete secular Hamiltonian approximation \mathcal{H}_{sec} (compare Figs. 1 and 12). For this reason we do not analyze in detail this model¹⁰, and we pass to determine and study the integrable normalized Hamiltonian with $N_P = 3$ and $N_{bk} = 4$, following the procedure explained in Section 3.3.

4.2.2 Normalized integrable octupolar approximation

First step. Following section 3.3, we start writing the octupolar approximation of the Hamiltonian as

$$\mathcal{H}_{sec}^{(N_P=3, N_{bk}=4)}(w_2, w_3, W_2, W_3) = \mathcal{H}_{int}^{(N_P=3, N_{bk}=4)}(\psi, W_2, W_3) + \mathcal{H}_{1,space}^{(N_P=3, N_{bk}=4)}(\psi, \varphi, W_2, W_3)$$

and we explicitly write the integrable part as

$$\mathcal{H}_{int}^{(N_P=3, N_{bk}=4)} = Z_0^{(N_P=3, N_{bk}=4)}(W_2, W_3) + \lambda Z_{0,1}^{(N_P=3, N_{bk}=4)}(\psi, W_2, W_3)$$

with

$$Z_0^{(N_P=3, N_{bk}=4)}(W_2, W_3) = c + aW_2 + bW_3.$$

⁹Look at formula (79) of [12] and follows *Step 2-Step 4* described in Section 2.3 of the same article.

¹⁰The analysis of such a kind of sequence of bifurcation is analogous to the one already studied in Section 3.3 and that will be done in the next Section, it is just inverted.

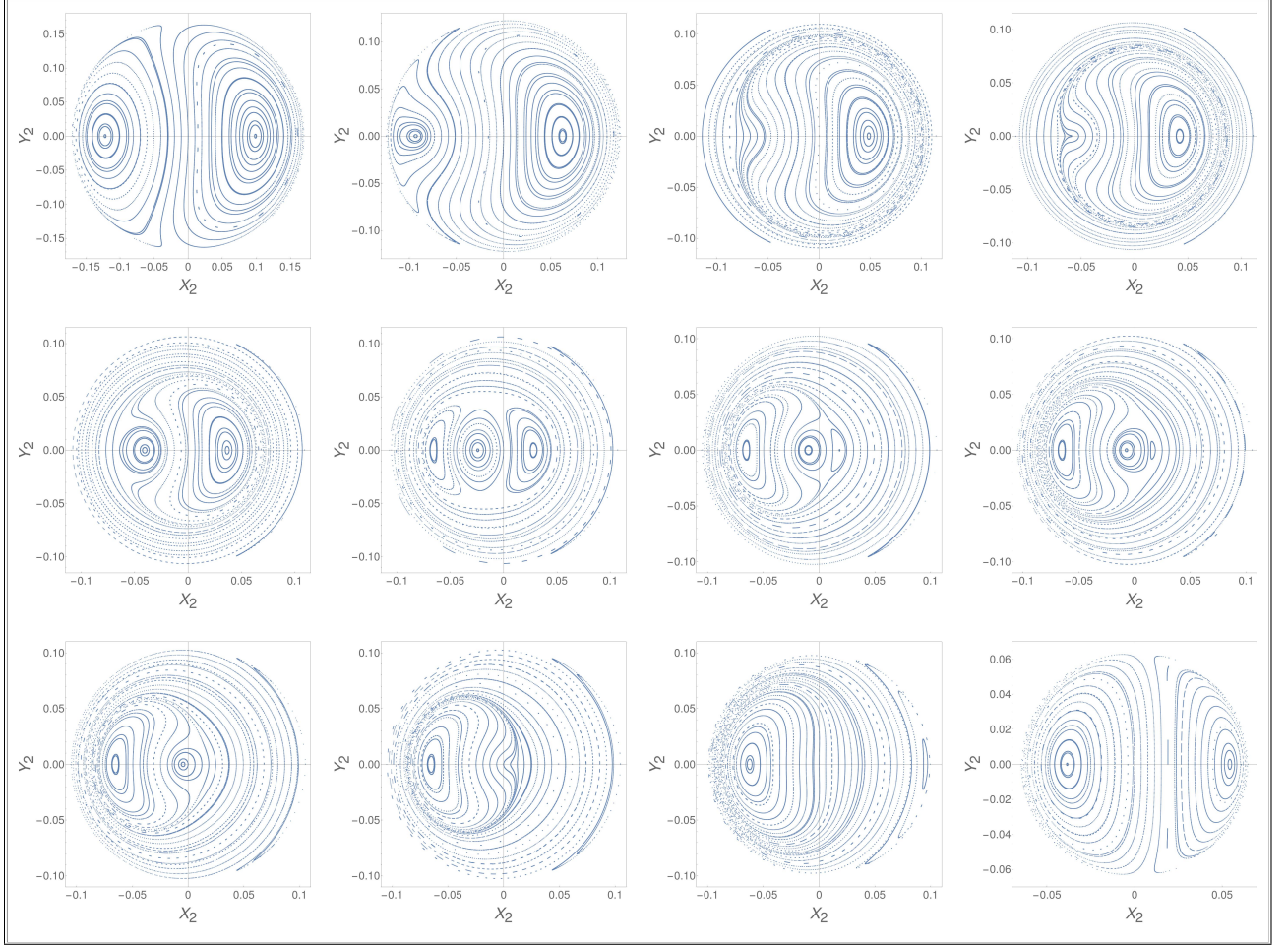


Figure 12: Poincaré surfaces of section $\mathcal{P}_{int}^{(N_P=3, N_{bk}=4)}(\mathcal{E}; \text{AMD})$ in the plane (X_2, Y_2) with L_z fixed and different values of energy. The surfaces of section are computed by a numerical integration of trajectories of the integrable part of the Hamiltonian truncated at multipolar degree $N_P = 3$, order $N_{bk} = 4$ in the eccentricities and energies (from top to bottom, from left to right) $\mathcal{E} = -5.83 \cdot 10^{-5}, -2.26 \cdot 10^{-5}, -1.78 \cdot 10^{-5}, -1.66 \cdot 10^{-5}, -1.57 \cdot 10^{-5}, -1.48 \cdot 10^{-5}, -1.43 \cdot 10^{-5}, -1.426 \cdot 10^{-5}, -1.42 \cdot 10^{-5}, -1.4 \cdot 10^{-5}, -1.22 \cdot 10^{-5}, -4.06 \cdot 10^{-6}$.

Thus, performing the above mentioned normalization, we end up (according to Eq. (35)) with

$$\tilde{\mathcal{H}}_{int}^{(N_P=3, N_{bk}=4)}(w_2 - w_3, W_2, W_3) = \mathcal{H}_{int}^{(N_P=3, N_{bk}=4)} + \left(\frac{\lambda}{2} \{ \mathcal{H}_{1,space}^{(N_P=3, N_{bk}=4)}, \chi \} \right) (w_2 - w_3, W_2, W_3). \quad (43)$$

In the Hopf variables, the above Hamiltonian (apart from constants) can be written as:

$$\tilde{\mathcal{H}}_{int}^{(N_P=3, N_{bk}=4)} = A\sigma_1^2 + C\sigma_3^2 + B\sigma_1\sigma_3 + D(\sigma_0)\sigma_1 + E(\sigma_0)\sigma_3 + F(\sigma_0) \quad (44)$$

where the coefficients, in our numerical example, are given by:¹¹

$$\begin{aligned} A &= 0, & C &= -0.0283636, \\ B &= -0.029019, & D(\sigma_0) &= 0.0011798 - 0.21118 \sigma_0, \\ E(\sigma_0) &= 0.00153399 - 0.270077 \sigma_0, & F(\sigma_0) &= -0.00010201 \sigma_0 - 0.42951 \sigma_0^2. \end{aligned}$$

The quadratic form $A\sigma_1^2 + C\sigma_3^2 + B\sigma_1\sigma_3$ yields hyperbola also in this case.

Second step. In order to determine the bifurcation values of σ_0 related to the CPs1 and CPs2, we use Eqs. (40) and (41) (following Section 4.1). Thus, first we need to perform a rotation so that $\mathcal{B} = 0$ (see Eq. (36) and the following discussion). So, we determine a change of coordinates $(\sigma_0, \sigma_1, \sigma_2, \sigma_3) \rightarrow (\tilde{\sigma}_0, \tilde{\sigma}_1, \tilde{\sigma}_2, \tilde{\sigma}_3)$ such that $\sigma_0 = \tilde{\sigma}_0$, $\sigma_2 = \tilde{\sigma}_2$ and

$$\sigma_1 = \alpha\tilde{\sigma}_1 + \beta\tilde{\sigma}_3, \quad \sigma_3 = -\beta\tilde{\sigma}_1 + \alpha\tilde{\sigma}_3$$

and α and β are computed so that

$$\alpha^2 + \beta^2 = 1 \quad \text{and} \quad B\alpha^2 + 2A\alpha\beta - 2C\alpha\beta - B\beta^2 = 0$$

(where A, B, C are described in Eq. (44)). Finally, in the “new” (i.e., rotated) coordinates $(\tilde{\sigma}_0, \tilde{\sigma}_1, \tilde{\sigma}_2, \tilde{\sigma}_3)$, the Hamiltonian takes the form of (36) with $\mathcal{B} = 0$.¹² Recalling the Poisson algebra structure of the variables $(\sigma_0, \sigma_1, \sigma_2, \sigma_3)$ and the change of coordinates $\tilde{\sigma}_1 = \alpha\sigma_1 - \beta\sigma_3$, $\tilde{\sigma}_3 = \beta\sigma_1 + \alpha\sigma_3$, it is easy to prove that the coordinates $(\tilde{\sigma}_0, \tilde{\sigma}_1, \tilde{\sigma}_2, \tilde{\sigma}_3)$ still satisfy the condition of sphere (21) and the Poisson algebra $\{\tilde{\sigma}_i, \tilde{\sigma}_j\} = -2\epsilon_{ijk}\tilde{\sigma}_k$, $i, j, k = 1, 2, 3$. Moreover $\sigma_0 = \tilde{\sigma}_0$ and it is a Casimir invariant of the previous algebra. Thus, compute the values of $\tilde{\sigma}_0$ for which the CP occur (i.e, solving Eqs. (40) and (41)) is equivalent to find the radius σ_0 for which the sphere and the hyperbola $\tilde{\mathcal{H}}_{int}^{(N_P=3, N_{bk}=4)}$ (Eq. (44)) are tangent.¹³

Third step. We are now ready to analyze the sequence of bifurcations produced by the study of the Poincaré surface of section of the Hamiltonian $\tilde{\mathcal{H}}_{int}^{(N_P=3, N_{bk}=4)}$ (Eq. (44)), at fixed different (decreasing) values of σ_0 (see Figs. 13a, 13b, 13c, 13d). The procedure is the same already explained at the end of Section 3.2.1 and already applied to the integrable Hamiltonian with $N_P = 5$, $N_{bk} = 12$ (in Sections 3.2.2) and to the normalized one (in Section 3.3.1).

¹¹Observe that, also in this case, $A = 0$, since there have not been produced terms of the form $\cos(2\omega_2 - 2\omega_3)$ up to order $\mathcal{O}(\varepsilon^4)$. However, if we had increased the book keeping order $N_{bk} > 4$, the term $\cos(2\omega_2 - 2\omega_3)$ would have been produced.

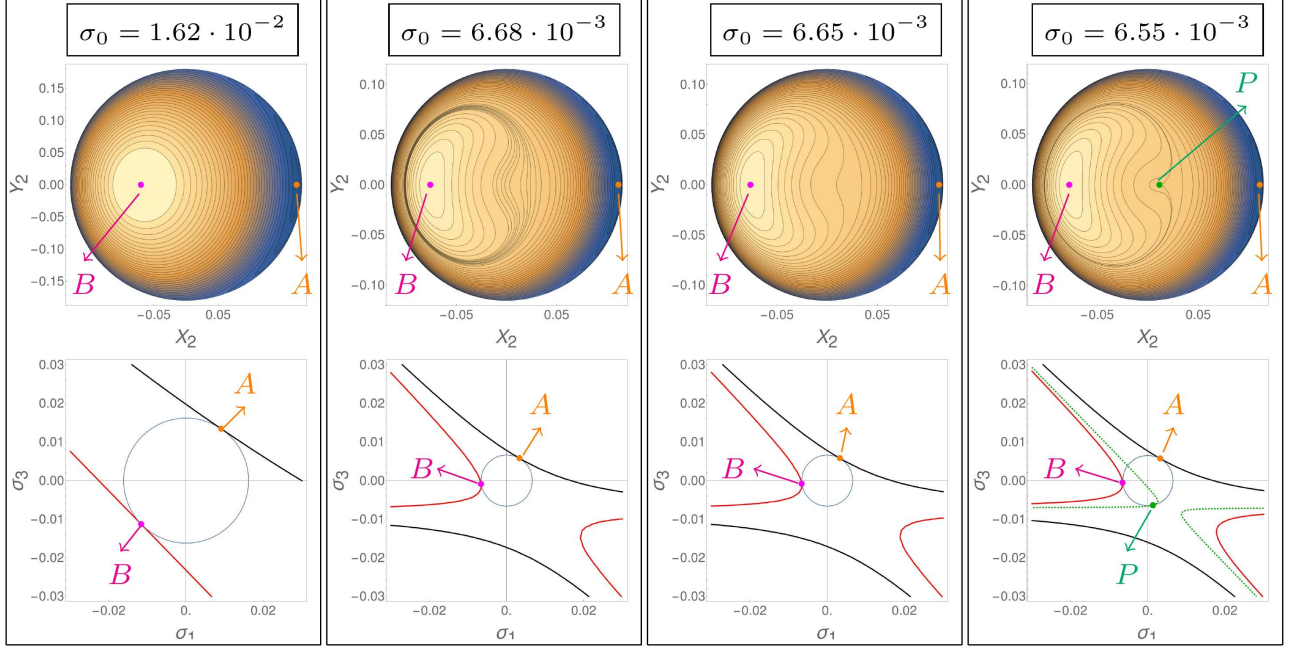
¹²In our numerical example (apart from constants and a term depending only on σ_0 , that is $-0.00010201\sigma_0 - 0.42951\sigma_0^2$), the Hamiltonian $\tilde{\mathcal{H}}_{int}^{(N_P=3, N_{bk}=4)}$ of Eq. (44), is described by

$$\mathcal{K}_I(\tilde{\sigma}_1, \tilde{\sigma}_3; \sigma_0) = \tilde{\mathcal{H}}_{int}^{(N_P=3, N_{bk}=4)} = \mathcal{A}\tilde{\sigma}_1^2 + \mathcal{C}\tilde{\sigma}_3^2 + (\mathcal{D}_1\sigma_0 + \Delta_1)\tilde{\sigma}_1 + (\mathcal{D}_3\sigma_0 + \Delta_3)\tilde{\sigma}_3 \quad (45)$$

with

$$\begin{aligned} \mathcal{A} &= 0.00610734, & \mathcal{C} &= -0.0344709, & \mathcal{D}_1 &= -0.089863, \\ \Delta_1 &= 0.000492281 & \mathcal{D}_2 &= -0.330852, & \Delta_2 &= 0.00187156. \end{aligned}$$

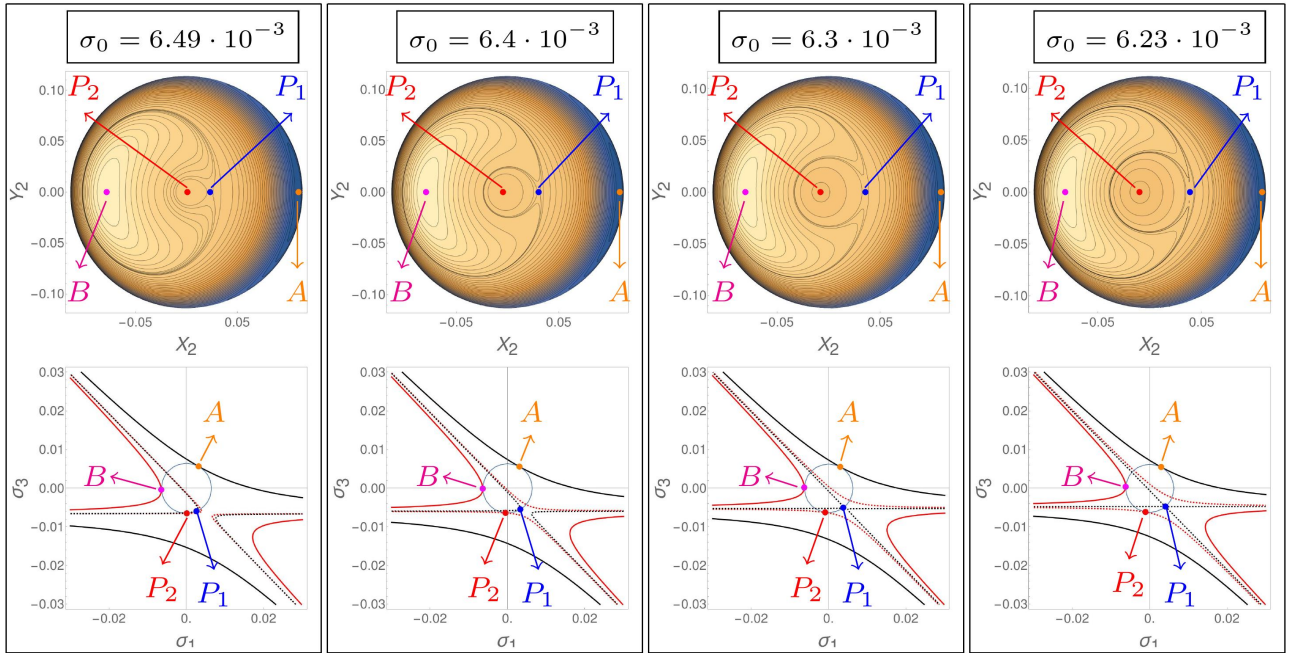
¹³In our numerical example, after having obtained the rotated Hamiltonian described in footnote 12 by Eq. (45), we solve Eqs. (40) and (41) to find the *bifurcation values* of σ_0 related, respectively, to CP of the first and second kind. We find that the numbers of CP1 change for $\sigma_0^{(CP1,1)} = 0.00489265$ and $\sigma_0^{(CP1,2)} = 0.00655611$, while the values $\sigma_0^{(CP2,1)} = 0.00623676$ and $\sigma_0^{(CP2,2)} = 0.00497142$ correspond to the appearance/disappearance of CP2, entering/leaving the circle $\sigma_1^2 + \sigma_3^2 = \sigma_0^2$ in the plane $\sigma_2 = 0$ (on the sphere, two CPs of the second kind bifurcate from/off a critical point of first kind corresponding to a tangency on the plane $\sigma_2 = 0$).



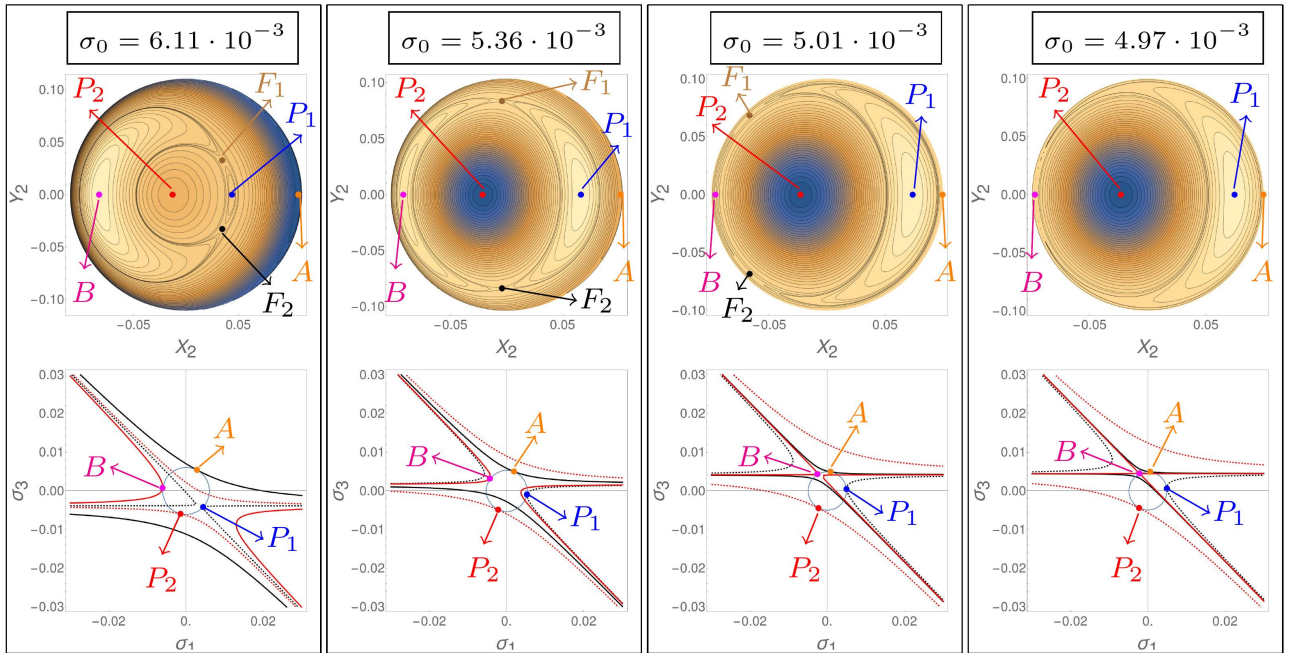
(a)

Figure 13

In the first frame of Fig. 13a we observe the presence of the apsidal corotation orbits. According to the notation already introduced in the previous sections, we find that \mathcal{S}_{σ_0} and $\mathcal{C}_{\sigma_0, \mathcal{E}}$ (where $\sigma_0 = \sigma_{0_{max}} = 1.62 \cdot 10^{-2}$) have two tangency points, A and B, respectively for $\mathcal{E} = \mathcal{E}_{min} = -1.816 \cdot 10^{-4}$ and $\mathcal{E} = \mathcal{E}_{2,3} = -6.37 \cdot 10^{-5}$. Starting from the second frame of the same Figure, it is evident the hyperbolic shape of $\mathcal{C}_{\sigma_0, \mathcal{E}}$. The fourth frame corresponds to the bifurcation value $\sigma_0^{(CP1,2)} = 0.00655611$ (see footnote 13), being one of the two solutions of Eq. (40). This means that, while in the third frame we have two tangency points between \mathcal{S}_{σ_0} and $\mathcal{C}_{\sigma_0, \mathcal{E}}$, instead, for $\sigma_0 = \sigma_0^{(CP1,2)}$ we have three fixed points, called A, B and P , that is the *bifurcation point*. Decreasing the value of σ_0 (first frame of Fig. 13b), we can observe that the bifurcation point P gives rise to two new fixed points of the Poincaré map, corresponding to periodic orbits called P_1 and P_2 ; thus, for such a value of σ_0 , we have four tangency points. More precisely, looking the passage between the fourth and the first bottom panels, respectively, of Fig. 13a and Fig. 13b, it is evident that the green hyperbola $\mathcal{C}_{\sigma_0^{(CP1,2)}, \mathcal{E}}$, that is tangent in one point to $\mathcal{S}_{\sigma_0^{(CP1,2)}}$ (correspondent to P in the section), gives rise to two new different hyperbolas, one (the red dashed one) with an ‘outer’ tangency with \mathcal{S}_{σ_0} (corresponding to the stable fixed point P_2) and the other (the black dashed one) with an ‘inner’ tangency with \mathcal{S}_{σ_0} (corresponding to the unstable fixed point P_1). Continuing to decrease the value of σ_0 (look at the passage between the bottom panels of Fig. 13b) we realize that the branches of the black dashed hyperbola (having the tangency point in P_1) become closer and closer. Corresponding to the fourth panel, they touch each other, and the hyperbola makes two planes whose center is a straight line piercing the sphere \mathcal{S}_{σ_0} . This happens for $\sigma_0 = \sigma_0^{(CP2,1)}$ (see footnote 13), that is described in (41). This corresponds to the case in which CPs of the second kind bifurcate from a CP of the first kind (P_1) on the plane $\sigma_2 = 0$.



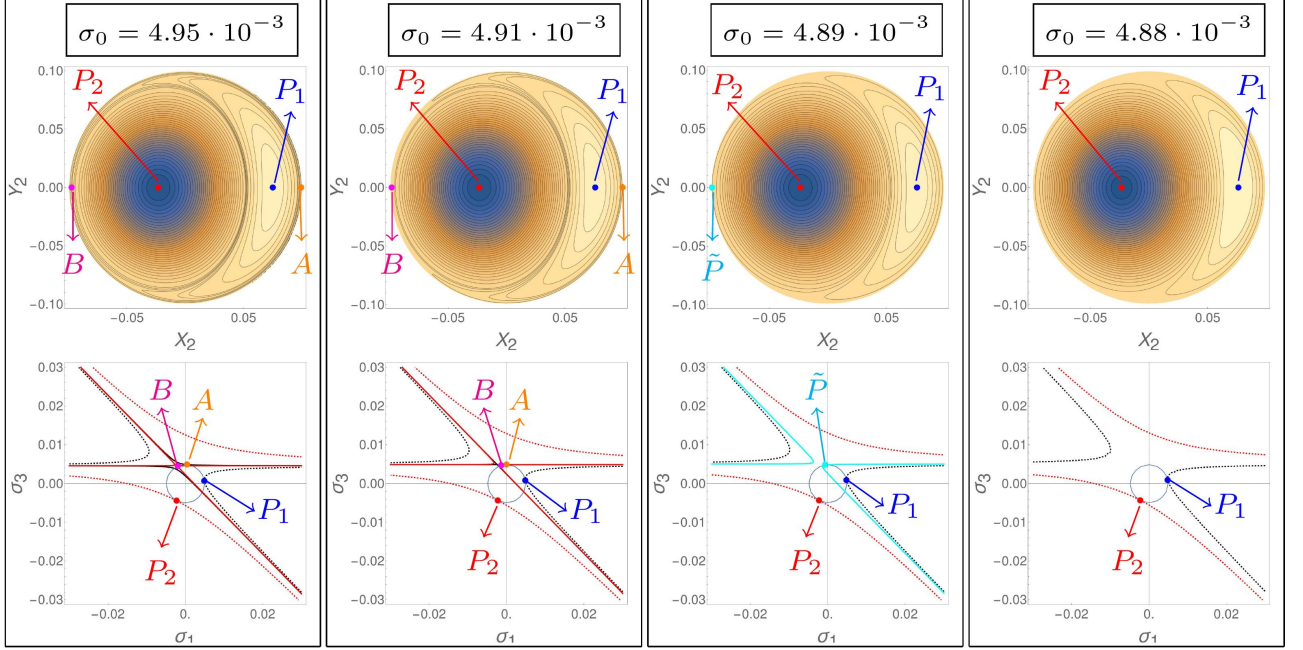
(b)



(c)

Figure 13

Decreasing again σ_0 (look at the first panel of Fig. 13c) we can notice that P_1 becomes stable



(d)

Figure 13: Analogously to Figure 9, the first rows of Figs. 13a, 13b, 13c and 13d show the contour plots, correspondent to $Y_3 = 0, \dot{Y}_3 \geq 0$, of $\tilde{\mathcal{H}}_{int}^{(N_P=3, N_{bk}=4)}(X_2, Y_2; \sigma_0) = \mathcal{E}$ (see Eq. (44) and proceed as explained at the end of section 3.2.1) in the plane (X_2, Y_2) and decreasing values of σ_0 (as explicitly indicated in the top of each frame). The fixed points of the flow have been outlined with colored points and have been calculated through the tangency method explained in the text (i.e. solving Eqs. (26) and (27) and expliciting the solutions in the Poincaré variables (X_2, Y_2) correspondently to the section $Y_3 = 0, \dot{Y}_3 \geq 0$). Instead, in the second rows of Figs. 13a, 13b, 13c and 13d there are reported the intersections of the sphere \mathcal{S}_{σ_0} (represented in blue) and of the energy surfaces $\mathcal{C}_{\sigma_0, \mathcal{E}}$ with the plane (σ_1, σ_3) for $\sigma_2 = 0$, for different values of the energy \mathcal{E} and values of σ_0 fixed as in the frame. Finally, we represent the energy surface $\mathcal{C}_{\sigma_0, \mathcal{E}}$ as a continued black/ continued red/ dashed black/ dashed red curve correspondingly to the tangency points A, B, P_1 , P_2 . See the text for more explanation.

by a pitchfork bifurcation, giving rise to two new unstable fixed points (CP2) F_1 and F_2 , out of the plane $\sigma_2 = 0$ and representing the points at which the line of intersection of the planes (i.e. where the two branches of the hyperbola touch each other) pierces the sphere. For still smaller value of σ_0 (see the second and third frame of Fig. 13c) the fixed points F_1 and F_2 move away from the fixed point of the orbit P_1 while later, for still smaller value of σ_0 (fourth frame of Fig. 13c), they collide with the B mode. This terminates the F -family of periodic orbits, by an inverse pitchfork bifurcations which renders the point B unstable. More precisely, the fourth panel correspond to the bifurcation value $\sigma_0 = \sigma_0^{(CP2,2)}$ (Eq. (41) and footnote 13); it corresponds to the value of the radius for which the F -family collides in a single point in the plane $\sigma_2 = 0$, i.e. bifurcates off the critical point of the first kind B, rendering it not stable anymore. For a 3D representation of the F -family, see Fig. 14.

Finally, from the first panel of Fig. 13d we can notice that B has become unstable (look also at the internal tangency shown at the bottom) and that, decreasing the value of σ_0 , the hyperbolas tangent, respectively, in B (the red one) and in A (the black one), becomes closer and closer, until when they collide in a single hyperbola (the cyan one, shown in the third panel of the same Figure). In fact, for

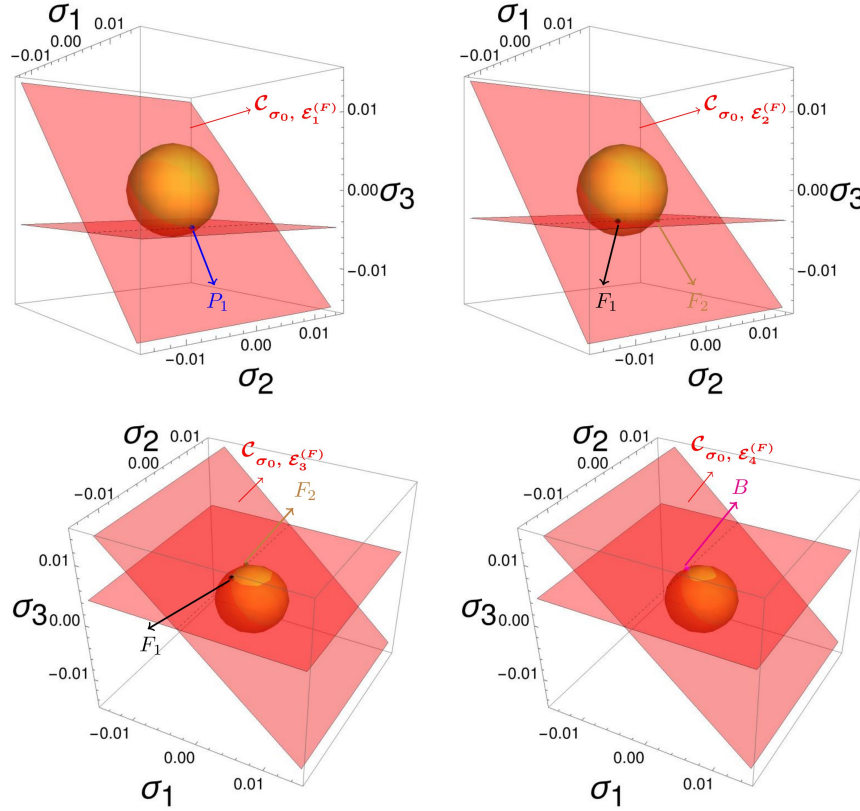


Figure 14: Graphical representation of the critical points of second kind F_1 and F_2 , for decreasing values of σ_0 (from top to bottom, from left to right). Top, left: 3D representation of the sphere S_{σ_0} and the surface $C_{\sigma_0, \mathcal{E}_1^{(F)}}$, in the case of bifurcation value $\sigma_0 = \sigma_0^{(CP2,1)} = 6.23 \cdot 10^{-3}$ (look at the last panel of Fig. 13b), where $\mathcal{E}_1^{(F)} = -1.7 \cdot 10^{-5}$ represents the energy of the mode P_1 . This is the critical value of σ_0 for which the critical points of the second kind F_1 and F_2 bifurcate from P_1 , on the plane $\sigma_2 = 0$. Top, right: As before, but in the case of a smaller value of the radius $\sigma_0 = 6.11 \cdot 10^{-3}$. For a value of the energy, namely $\mathcal{E}_2^{(F)} = -1.66 \cdot 10^{-5}$, $C_{\sigma_0, \mathcal{E}_2^{(F)}}$ pierces the sphere S_{σ_0} in the points F_1 and F_2 of coordinates, respectively, $(\sigma_1^{(F)}, \sigma_2^{(F)}, \sigma_3^{(F)})$ and $(\sigma_1^{(F)}, -\sigma_2^{(F)}, \sigma_3^{(F)})$. Bottom, left: As before, but in the case of a smaller value of the radius $\sigma_0 = 5.01 \cdot 10^{-3}$. For a value of the energy, namely $\mathcal{E}_3^{(F)} = -1.1 \cdot 10^{-5}$, the surface of the energy pierces the sphere in the F -modes. Observe that, with respect to the previous picture, the F -family is moving away, towards the left part of the picture. Bottom, right: As before, in the case of bifurcation value $\sigma_0 = \sigma_0^{(CP2,2)} = 4.97 \cdot 10^{-3}$ (look at the last panel of Fig. 13c), where $\mathcal{E}_4^{(F)} = -1.08 \cdot 10^{-5}$ represents the energy of the mode B . This is the critical value of σ_0 for which F_1 and F_2 collide in the B point, terminating (by an inverse bifurcation) the F -family.

$\sigma_0 = \sigma_0^{(CP1,1)} = 4.89 \cdot 10^{-3}$ the points A and B collide in one single point, that is a *bifurcation point*, called \tilde{P} . So, the number of tangency points passes from four (A, B, P_1, P_2) to three (\tilde{P}, P_1, P_2) and for smaller values of σ_0 passes to two. Thus, finally, the only stable points surviving to the chain of bifurcations are P_2 and P_1 .

5 Conclusions

The main goal of this work is twofold: analyze the sequence of bifurcations produced by integrable Hamiltonian approximations and determine an effective normal form able to qualitatively capture the sequence of bifurcation of a complete secular Hamiltonian. After normalization, we reduce to the normal form of a 1 : 1 resonance expressed in the Hopf variables [3, 5, 16]. The novelty of the approach consists not only in the construction of this integrable normal form, but also in the ability to provide semi-analytical quantitative predictions of the bifurcations through a geometric reduction [2, 6, 11]. The concluding remarks and results of the work are summarized in the following:

- i. In Section 3.2.1, we show that the periodic orbits of an integrable Hamiltonian system can be found simply computing the tangencies between two surfaces, namely, the sphere \mathcal{S}_{σ_0} and the energy surface $\mathcal{C}_{\sigma_0, \varepsilon}$. According to the coefficients and parameters involved in the Hamiltonian model, the last surface $\mathcal{C}_{\sigma_0, \varepsilon}$ can represent different kinds of surfaces: for instance, in Section 3.2.2, we see that it is an ‘elliptic-like’ surface, while in Section 3.3.1 we see it is an ‘hyperbolic-like’ surface. Observing, for example, Figures 5 and 9, it is evident that this difference can lead to different sequences of bifurcations and also to a different nature of the arising periodic orbits, that can be either stable or unstable. For example, we see from Fig. 5 that, in the first case (the ‘elliptic-like’ one), the pitchfork bifurcation is generated by the A mode, and the corresponding F modes are stable. Instead in the second case (the ‘hyperbolic-like’ one, shown in Fig. 9) the pitchforks are generated by the P_1 mode and they have an unstable behaviour. In conclusion, changing the level of the integral σ_0 , we can analyze in details the sequence of bifurcations, looking at the evolution of the surfaces \mathcal{S}_{σ_0} and $\mathcal{C}_{\sigma_0, \varepsilon}$ in the space and studying their contacts. The power of this analysis is that each periodic orbits, namely the apsidal corotation, the saddle-node and the pitchfork, can be easily visualized in the 3D space and seen as the result of the contacts between these two surfaces, acquiring a deep geometric interpretation.
- ii. In Section 3.2 we have analyzed the sequence of bifurcation in the integrable Hamiltonian approximation, i.e. considering just \mathcal{H}_{int} , and we have outlined that it leads to a different sequence of bifurcations with respect to the secular Hamiltonian approximation (whose sequences are reported in Fig. 1). However, in Section 3.3 we have presented an integral normal form, i.e. a new integrable Hamiltonian approximation $\mathcal{H}_{int}^{(1)}$, where the original integrable Hamiltonian \mathcal{H}_{int} is enriched by a contributing term, given by just one step of the normalization algorithm (see Eq. (35)). Considering this new simple Hamiltonian we are able to *qualitatively* reproduce the same sequence of bifurcations of the complete system (see Fig. 8). Moreover, thanks to the introduction of this normal form, we show that, in order to *qualitatively* reproduce the sequence of bifurcations of the complete system, it is sufficient to limit the study to a lower-order approximation of the Hamiltonian, both in the multipolar order N_P (that we decreased from 5 to 3) and in order of the eccentricity N_{bk} (that we decreased from 12 to 4), as shown in Section 4.2.2.
- iii. Given a general integrable Hamiltonian, of the form described by Eq. (36), we find analytical formulae giving the *bifurcation value* of the integral giving rise to the saddle-node and pitchfork bifurcations. More precisely, the bifurcation value of σ_0 can be numerically found from equation (40) (depending only on the generic coefficients of the Hamiltonian) for critical points of the first kind and are analytically found, in Eq. (41), for critical points of the second kind. In Section 4.2.2 we apply these formulae to find the bifurcation values of the integral σ_0 for the

normalized integrable Hamiltonian $\tilde{\mathcal{H}}_{int}^{(N_P=3, N_{bk}=4)}$, explicitly described by Eq. (45) (footnote 12). From Fig. 13 we can appreciate how our formulæ predict precisely the birth of the saddle-node and pitchfork bifurcations. We want to stress the fact that, in the example we considered (i.e., a Hamiltonian model in which orbital parameters compatible with those observed in the ν -Andromeæ system are considered) we expect the bifurcation values of the integral, giving rise to the CP1 and CP2, to be not so close to the values for which the saddle-node and pitchfork bifurcations of the real system occur. This is because we are dealing with a not-hierarchical spatial problem. However, we want to outline that, as explained by Migaszewski and Goździewski in [13], the shape of the secular Hamiltonian depends significantly on the ratio of the semi-major axis $\alpha = a_2/a_3$, in particular in the spatial problem. Moreover, as outlined in their work, for hierarchical system the octupolar expansion is sufficient to reproduce the real dynamics (see also [4] and [15]). So, if a hierarchical system is considered, it is possible to simply determine its octupolar Hamiltonian approximation to describe its dynamical behaviour. If interested in finding the periodic orbits of the integrable Hamiltonian (that is the first step to proceed with a perturbation treatment of the full octupolar Hamiltonian), our formulae allow to find the precise level of the integral giving rise to the bifurcation points. Moreover, it is possible to proceed with one or more steps of the normalization procedure we presented in Section 3.3 and apply the above formulæ for a ‘more accurate’ integrable Hamiltonian approximation.

References

- [1] C. Beaugé, S. Ferraz-Mello, and T. Michtchenko. Extrasolar planets in mean-motion resonance: apses alignment and asymmetric stationary solutions. *The Astrophysical Journal*, 593(2):1124–1133, 2003.
- [2] D. Carrasco, J. F. Palacián, C. Vidal, J. Vidarte, and P. Yanguas. Dynamics of axially symmetric perturbed Hamiltonians in 1:1:1 resonance. *Journal of Nonlinear Sciences*, 28:1293–1359, 2018.
- [3] R. H. Cushman and L. M. Bates. *Global aspects of classical integrable systems*, volume 94. Springer, 1997.
- [4] E. B. Ford, B. Kozinsky, and F. A. Rasio. Secular evolution of hierarchical triple star systems. *The Astrophysical Journal*, 535(1):385–401, 2000.
- [5] H. Hansmann and I. Hoveijn. The 1:1 resonance in Hamiltonian systems. *Journal of Differential Equations*, 266(11):6963–6984, 2019.
- [6] M. Kummer. On resonant non linearly coupled oscillators with two equal frequencies. *Communications in Mathematical Physics*, 48:53–79, 1976.
- [7] J. Laskar and P. Robutel. Stability of the planetary three-body problem. *Celestial Mechanics and Dynamical Astronomy*, 62(3):193–217, 1995.
- [8] G. Laughlin, J. Chambers, and D. Fischer. A dynamical analysis of the 47 Ursae Majoris planetary system. *The Astrophysical Journal*, 579(1):455–467, 2002.
- [9] M. H. Lee and S. Peale. Secular evolution of hierarchical planetary systems. *The Astrophysical Journal*, 592(2):1201–1216, 2003.

- [10] M. L. Lidov and S. Ziglin. Non-restricted double-averaged three body problem in Hill’s case. *Celestial Mechanics*, 13(4):471–489, 1976.
- [11] A. Marchesiello and G. Pucacco. Bifurcation sequences in the symmetric 1:1 Hamiltonian resonance. *International Journal of Bifurcation and Chaos*, 26(04):1630011, 2016.
- [12] R. Mastroianni and C. Efthymiopoulos. The phase-space architecture in extrasolar systems with two planets in orbits of high mutual inclination. *Celestial Mechanics and Dynamical Astronomy*, 135(3):22, 2023.
- [13] C. Migaszewski and K. Goździewski. The non-resonant, relativistic dynamics of circumbinary planets. *Monthly Notices of the Royal Astronomical Society*, 411(1):565–583, 2011.
- [14] S. Naoz. The eccentric Kozai-Lidov effect and its applications. *Annual Review of Astronomy and Astrophysics*, 54:441–489, 2016.
- [15] S. Naoz, W. M. Farr, Y. Lithwick, F. A. Rasio, and J. Teyssandier. Secular dynamics in hierarchical three-body systems. *Monthly Notices of the Royal Astronomical Society*, 431(3):2155–2171, 2013.
- [16] J. C. van der Meer. Generic one-parameter versal unfoldings of symmetric Hamiltonian systems in 1:1 resonance. *International Journal of Pure and Applied Mathematics*, 53(4):547–561, 2009.